

UNIVERSITY OF CAPE TOWN

MASTER'S DISSERTATION

Toward a Full Aircraft Model Platform for Fuel Slosh-Structure Interaction Simulations

Author:

Javon Farao

Supervisor:

Prof. Arnaud MALAN

Co-Supervisor:

Mr. Francesco GAMBOLI

A thesis submitted to University of Cape Town in candidature for the degree of
Master of Science in Engineering

Department of Mechanical Engineering
Computational Fluid Dynamics Research Group

March 2015



The copyright of this thesis vests in the author. No quotation from it or information derived from it is to be published without full acknowledgement of the source. The thesis is to be used for private study or non-commercial research purposes only.

Published by the University of Cape Town (UCT) in terms of the non-exclusive license granted to UCT by the author.

Declaration of Authorship

I, Javon FARAO, declare that this dissertation titled, 'Toward a Full Aircraft Model Platform for Fuel Slosh-Structure Interaction Simulations' and the work presented in it are my own. I confirm that:

- This work was done wholly or mainly while in candidature for a research degree at this University.
- Where any part of this dissertation has previously been submitted for a degree or any other qualification at this University or any other institution, this has been clearly stated.
- Where I have consulted the published work of others, this is always clearly attributed.
- I know the meaning of plagiarism and declare that all the work in the document, save for that which is properly acknowledged, is my own.

Signed:

Date:

*This work is dedicated to my parents,
Jafta and Faesa Farao.*

Abstract

The purpose of this study was to initiate the development of a full aircraft model (FAM) for the purpose of non-linear loads calculation of an aircraft. The FAM is employed during the design process of an aircraft and comprises of various reduced-order models (ROMs). These are mainly structural, slosh and aerodynamic loads. This study focused on the structural and slosh aspects using *Elemental*TM software as the base. First, a structural ROM was developed such that it is compatible with Airbus data and processes. The developed code reads in MSC Nastran data, from which Hermitian finite element discretisation is performed followed by transient calculations. To this end, the structure was represented by Timoshenko beam theory. The structural ROM was validated and verified against the widely used MSC Nastran commercial software. Simulated dynamic responses were within 5% while eigenvalue predictions were within 2% of each other. Secondly, a strongly-coupled partitioned fluid-structure interaction (FSI) scheme was deployed to incorporate the high-fidelity sloshing fluid onto the structure. Lastly, the developed FSI technology was verified and validated against challenging analytical as well as real-world benchmark test cases. It was demonstrated to be accurate and robust in all cases.

Acknowledgements

For as long as I can remember I aspired to design, build and fly aircraft. This project has exceeded my wildest dreams. I have been able to work with individuals at the forefront of engineering application in the field of aeronautics and CFD. I thus wish to acknowledge the following people for their contribution and assistance during the process of the project, as without them the successful completion of this project would not have been possible.

Firstly, I would like to extend my heartfelt gratitude to Professor Arnaud Malan. Your unwavering patience and valuable insight has enabled me to exceed any personal growth expectations I harboured at the start of this journey. You possess a 'Midas' touch that stems from your wealth of knowledge and willingness to go the extra mile for students. Secondly, I would like to thank Mr. Francesco Gambioli, from Airbus UK, whose insight and experience has not only enhanced this project but also my growth as a critical thinker. I also acknowledge and appreciate the effort undertaken to organise the trip to Airbus headquarters in Toulouse, France, to present my work. The funding obtained from Airbus and the NAC is acknowledged and duly appreciated.

To the UCT Computational Fluid Dynamics Industrial Research Group, thank you for your advice, daily office debates and general banter. Special recognition must go to Mr. Andrew Mowat who was there throughout all the trying times and major breakthroughs. Thank you for always sacrificing your time to guide, mentor, assist and critically evaluate any ideas throughout the project. Gratitude and appreciation is also expressed to my extended family and friends, for your support, prayers and encouragement throughout a very challenging period. Lastly, to my parents for their unconditional love, support and sacrifice, without whom none of this would have been possible.

Contents

Declaration of Authorship	i
Abstract	iii
Acknowledgements	iv
Contents	iv
List of Figures	vii
List of Tables	ix
Nomenclature	x
1 Introduction	1
1.1 Background and Project Motivation	1
1.2 Purpose and Overview of Study	3
1.3 Dissertation Layout	4
2 Structural Model Governing Equations	5
2.1 Introduction	5
2.2 Timoshenko Beam Theory	5
2.2.1 Problem Formulation	6
2.3 Conclusion	10
3 Structural Model: Numerical Discretisation	11
3.1 Introduction	11
3.2 Finite Element Method	12
3.3 Spatial Discretisation	13
3.3.1 Spatial discretisation of the Timoshenko beam	15
3.3.2 Boundary Conditions and Loading	18
3.4 Temporal Discretisation	19
3.4.1 Newmark Method	19
3.4.2 Modal Analysis	20
3.4.2.1 Cholesky Factorisation	22
3.4.2.2 Arnoldi Method	22
3.4.2.3 Modified Gram-Schmidt Decomposition	24

3.4.3	Damping Model	24
3.5	Conclusion	26
4	Structural Model: Verification and Validation	27
4.1	Introduction	27
4.2	Static Bending	27
4.3	2D Dynamic Beam	29
4.4	Eigen-Analysis	30
4.5	Airbus Structure	33
4.6	Conclusion	35
5	Fluid-Structure Interaction	36
5.1	Introduction	36
5.2	Fluid Governing Equations	37
5.3	Partitioned FSI Interface Treatment	38
5.3.1	Added-Mass Effect	39
5.3.2	Proposed Algorithm	39
5.4	Industrial Application	43
5.5	FSI Solution Procedure	46
5.6	Conclusion	46
6	Fluid-Structure Interaction: Results and Evaluation	47
6.1	Introduction	47
6.2	Piston-Channel Problem	47
6.3	Industrial Application	50
6.4	Conclusion	58
7	Summary, Conclusions and Recommendations	59
7.1	Summary and Conclusions	59
7.2	Recommendations	60
A	Matrix Computation	61
	References	63

List of Figures

2.1	Undeformed beam under distributed loading $q(x)$	6
2.2	Beam in the deformed configuration with differential element, dx , and deformed beam plane	6
2.3	Differential free body diagram of the forces and moments acting on the beam	7
2.4	Kinematics of the Timoshenko beam	7
3.1	Diagram of the finite element method on a 2D unstructured grid	11
3.2	Diagram of a general continuum body under loading	13
3.3	Diagram of the beam element with 12 degrees-of-freedom per element [31]	16
3.4	Mapping of a 1D domain from the physical domain $[a, b]$ to the parent domain $[-1, 1]$ [35]	16
3.5	Newmark's constant-average-acceleration scheme [33]	19
3.6	Illustration of a sparse, symmetric matrix with few non-zero values shown	21
3.7	Upper Hessenberg matrix structure	23
4.1	Cantilever beam under transverse load	27
4.2	Static deformation of a cantilever beam under transverse tip loading	28
4.3	Cantilever beam under applied shear	29
4.4	Cantilever dynamic response compared to analytical and <i>MSC Nas-tran</i>	30
4.5	Computed mode shapes of Timoshenko cantilever beam	31
4.6	Cited [43] mode shapes of Timoshenko cantilever beam	31
4.7	Dynamic response of the cantilever free end in time (red) and frequency domain (black)	32
4.8	Airbus condensed stick model	33
4.9	Right wing of Airbus structural ROM	34
4.10	Dynamic vertical displacement of right wing tip after being subjected to transient tip load.	34
5.1	Diagram of an aircraft with its center (blue) and wing fuel tanks (red)	36
5.2	Loosely-coupled partitioned FSI scheme	38
5.3	Sloshing tank section with zones (top) corresponding to an associated added mass on the structural ROM (bottom)	41

5.4	Proposed strongly-coupled partitioned FSI scheme	42
5.5	Top view representation of an Airbus aircraft wing and wing tanks .	43
5.6	Front view representation of an Airbus aircraft wing tanks	43
5.7	Diagram of an Airbus aircraft wing coupled to its center (red) and wing fuel tanks (blue)	44
5.8	Translational acceleration of the centre fuel tank	44
5.9	Rotational acceleration of the wing fuel tank	45
5.10	Gravitational acceleration components of the fuel tank	45
6.1	Piston-Channel problem with boundary conditions	48
6.2	Mathematical representation of the piston-channel problem	48
6.3	Displacement (left) and velocity (right) of the interface of the piston and channel	49
6.4	Displacement (left) and velocity (right) of the interface of the piston and channel with various time step sizes	49
6.5	Number of iterations required per time step for the mass residuals to converge	49
6.6	Real-life gust profile imposed as wing root acceleration (axes in terms of normalised acceleration and time)	50
6.7	Unstructured mesh for vertical sloshing (13,430 nodes)	50
6.8	Aircraft wing tanks with 75% fill level	51
6.9	Aircraft wing tanks with 25% fill level	51
6.10	Wing tip deflection in vertical (top), horizontal (middle) and along the fuselage (bottom) direction for various tank fill levels	53
6.11	Input gust compared to center and wing tank acceleration for 75% filled tank	54
6.12	Input gust compared to center and wing tank acceleration for 25% filled tank	55
6.13	Pressure locations of the center (blue) and wing (red) tanks	55
6.14	Normalised pressure at the identified tank locations for 75% (top) and 25% (bottom) fill level tanks	56
6.15	Interface representation of 75% filled tank at the various time steps	57
6.16	Interface representation of 25% filled tank at the various time steps	57

List of Tables

4.1	Cantilever Modal Analysis	30
4.2	Modal Dynamic Analysis Cost Savings	32
6.1	Table of fluid and gas properties at 12,000 <i>m</i> above sea-level	51

Nomenclature

Roman Symbols

a	Acceleration ($m.s^{-2}$)
A	Cross-sectional area (m^2)
\mathbf{b}	Body force (N)
\mathbf{B}	Strain matrix (derivative of a shape function matrix)
\mathbf{C}	Damping matrix
dx	Incremental length of an element
E	Elastic modulus (Pa)
f	Force (N)
g	Gravitational acceleration ($9.81 m.s^{-2}$)
G	Shear modulus (Pa)
I	Area moment of inertia (m^4)
J	Polar moment of inertia (m^4)
\mathbf{K}	Stiffness matrix
l	Length (m)
M	Moment due to applied force ($N.m$)
\mathbf{M}	Mass matrix
\mathbf{N}	Shape function matrix
V	Shear force (N)
p	Pressure (Pa)
$q(x)$	Distributed beam load ($N.m^{-1}$)
\mathbf{R}	Residual loads vector (N)
S	Enclosed surface (m^2)
t	Time (s)
T	Torsional force ($N.m$)
u	Deformation in principle directions (m)
\mathbf{u}	Virtual displacement vector (m)
U	Internal work (kJ)

\mathbf{U}	Nodal displacement vector (m)
$\dot{\mathbf{U}}$	Nodal velocity vector ($m.s^{-1}$)
$\ddot{\mathbf{U}}$	Nodal acceleration vector ($m.s^{-2}$)
V	Volume (m^3)
$w(x)$	Lateral displacement of the beam neutral axis
W	External work (kJ)
\mathbf{x}	Distance (m)

Greek Symbols

α	Newmark method constant
δ	Newmark method constant
ϵ	Strain of an element
γ	Shear angle of deformed beam
κ	Shear strain correction factor
λ	Eigen-value
ν	Poisson ratio
ω	Natural frequency ($rad.s^{-1}$)
Ω	Eigen-value matrix
ϕ	Eigen-vector
Φ	Eigen-vector matrix
ρ	Density ($kg.m^{-3}$)
τ	Stress loads (Pa)
θ	Angular rotation of the cross-section of an element (rad)
ξ	Coordinate in natural or transformed space
ζ	Damping ratios

Superscripts

τ	Pseudo time step number
n	Real time step number
T	Transpose of a matrix

Subscripts

a	Axial
b	Bending
B	Body
$cent$	Centrifugal

C	Concentrated node
e	Element
i	Principle direction
int	Interface
m	Order of a matrix
S	Surface
t	Torsional
$tang$	Tangential
x, y, z	Cartesian direction

Mathematical Operators

$det\bullet$	Determinant of \bullet
δ_{ij}	Kronecker delta operator: unity if $i = j$ and zero if $i \neq j$
$\partial\bullet$	Partial derivative of \bullet
$\delta\bullet$	Increment in \bullet
$\ \bullet\ _2$	L_2 error norm vector, \bullet
$[\bullet]^{-1}$	Inverse of a matrix, \bullet

Abbreviations

CFD	Computational Fluid Dynamics
EASA	European Aviation Safety Agency
EBBT	Euler-Bernoulli Beam Theory
EMM	Equivalent Mechanical Models
FAM	Full Aircraft Model
FSI	Fluid-Structure Interaction
POD	Proper Orthogonal Decomposition
ROM	Reduced-Order Model
SPH	Smooth Particle Hydrodynamics
TBT	Timoshenko Beam Theory

Chapter 1

Introduction

1.1 Background and Project Motivation

Air transport is one of the safest modes of travel due to the stringent certification process that is required by the European Aviation Safety Agency (EASA) and the Federal Aviation Authority (FAA). Fatality statistics peg commercial aircraft at only 0.0003 per 100 million passenger miles as compared to 0.61 for motor vehicles [1]. Additionally, the close adherence to the regulations enforced during design and manufacture result in the improved safety record. Airbus is the world's largest large passenger aircraft manufacturer with a commitment to reduce carbon emissions and produce safe, lighter and more fuel efficient aircraft. The company employs over 55,000 people and currently has more than 55% of all current commercial aircraft orders [2].

The European Aviation Safety Agency is responsible for drafting aviation safety legislation as well as certifying aeronautical products. In the interest of safety, the EASA requires an accurate assessment of the overall forces experienced by an aircraft. The design needs to encompass the entire flight envelope which includes numerous altitudes and flight velocities as well as various load conditions [3]. To achieve this requires millions of calculations. Due to comprehensive high resolution computational fluid dynamics (CFD) calculations being too expensive, if used in isolation, so-called reduced order models (ROMs) are employed. A ROM is a mathematical representation that constitutes the dominant physics of the system it approximates and should be capable of reproducing the dynamics of the full-order problem [4]. For the purpose of global loads calculation, Airbus employs a full aircraft model (FAM) which comprises of reduced-order-models for the structure, aerodynamic and sloshing effects respectively. ROMs, once trained or calibrated via selected full order CFD calculations, may be employed for accurate full envelope loads calculations.

An aircraft structure is complex, and a singular wing comprises of thousands of components. From a loads calculation point of view, the stress analysis on each component within the wing would be excessive, thus a structural ROM is sought.

The concept of reducing the order of the structure has been extensively studied [5][6]. Reduction techniques that remain popular in industry include Guyan reduction [7], proper orthogonal decomposition (POD) and static condensation [8]. Additionally, modal analysis has been deployed with success to construct ROMs of the structure [9][10], while also facilitating modelling in the frequency domain. These ROMs all exhibit linear characteristics which results in the motion (displacement) being described along a straight line. Nonetheless, these reduction techniques provide sufficient accuracy for many cases.

As noted previously, the loads calculation process requires accounting for fuel sloshing effects. This is particularly important as the mass of the fuel may be three times that of the wing mass. Sloshing occurs in a partially filled tank and can be defined as the motion of the liquid free-surface as a result of external tank excitation [11]. The dynamic fuel pressure on the tank walls, caused by the external excitation, vary significantly with excitation frequency, tank fill level and tank geometry. Various numerical methods exist to analyse the sloshing pressures, e.g. computational fluid dynamics modelling or smooth particle hydrodynamics (SPH), however these methods are computationally expensive [12]. Airbus currently utilises a conservative approach to account for slosh during loads calculation by means of a quasi-static method i.e. approximating slosh loads upon landing to be full fuel tanks acting as a rigid mass [13]. The development of the equivalent mechanical model (EMM) has aided in representing slosh with improved resolution [14], though greater accuracy is still sought. This is as the robust and accurate modelling of non-linear slosh via EMMs [14] [15] [16] and surrogate ROMs [17] are still elusive.

In the context of aircraft, the interaction between fuel and wing structure results in a coupled non-linear dynamic system known as fluid-structure interaction (FSI) [18]. Examples of this phenomenon include aero-elastic flutter [19] [20] and buffeting. FSI solution algorithms may be divided into the type of coupling that exists between the fluid and the structure namely, weak and strong coupling. Due to its computational efficiency, weak coupling is often employed for aircraft aero-elastic modelling [21]. However, when considering non-linear slosh interaction, this is no longer suitable from both a stability as well as conservation perspective [24]. Notwithstanding its benefits, numerical instabilities arise when using a time staggered approach in the context of aircraft loads predictions. It also does not impose conservation between fluid and structure at each time step [22]. Strongly-coupled modelling techniques, in contrast, invoke dynamic and kinematic continuity at the fluid-structure interface and may be solved via monolithic or partitioned methods [23]. The former method solves the problem with a single matrix while partitioned methods discretise the fluid and structural domains separately [22]. The major downside of the monolithic approach is that it requires the structure and slosh components to contribute to the same matrix to be solved, while requiring complex Jacobian calculations.

1.2 Purpose and Overview of Study

In context of the aforementioned, the purpose of this study is to develop a computational platform by which to conduct aircraft loads simulations with a high-resolution slosh model attached. This platform should therefore allow for determination of the dynamic response of an aircraft wing under numerous aerodynamic conditions and load configurations subject to non-linear slosh. As such, the structural component forms the basis of the loads analysis platform onto which the external loads are introduced. According to the author's knowledge there is currently no such tool available that incorporates non-linear high resolution slosh into the full aircraft model for loads analysis. In addition, this is to be done in such a way as to allow seamless integration into current Airbus loads analysis processes. In this regard, the data required by the structural ROM is to be read in via two formats viz. a beam model and a stiffness matrix (produced via Airbus MSC Nastran software). The latter, together with the aerodynamic ROM, is typically supplied by the 'Loads and Aeroelastics' department within the company.

Regarding the creation of a structural ROM via beam theory, Timoshenko beam theory is employed to represent the governing equations. These are discretised via the finite element method (FEM) with Hermitian shape functions. The implementation is done into *Elemental*TM, as this modelling software provides much of the required functionality. The beam model is to include the development of modal analysis procedures to determine the natural frequencies of vibration and modes of vibration. This analysis supports a stable time domain solution as well as the construction of a frequency domain structural ROM. A verification and validation is then performed on the structural ROM by comparing predicted results to analytical solutions as well as that of the MSC Nastran software.

With regards to the various load configurations during aircraft flight, fuel sloshing effects within the aircraft tanks require consideration during the loads analysis procedure. In order to compute the highly non-linear forces induced by the slosh, an in-house multi-physics CFD code, *Elemental*TM, will be employed. It utilises a vertex-centred, finite volume method to discretise the fluid domain. In order to incorporate the sloshing loads onto the computational structural platform, a strongly-coupled partitioned fluid-structure interaction scheme is proposed. The proposed scheme enables for stable and conservative coupling while being simple enough to integrate into existing Airbus loads calculation processes. Finally, the developed FSI platform is assessed by application to an analytical test-case as well as an actual Airbus wing under gust load conditions.

1.3 Dissertation Layout

The dissertation is divided into 7 chapters, including an introduction and conclusion. The following provides a short summary of each chapter.

- **Chapter Two: Structural Model: Governing Equations.**
The set of governing equations employed to describe the dynamics of the structure are detailed.
- **Chapter Three: Structural Model: Numerical Discretisation.**
The spatial and temporal discretisation algorithms of the structure and the modal analysis procedure for large, sparse matrices are described.
- **Chapter Four: Structural Model: Verification and Validation.**
The results of the verification and validation of the modelling technology developed are illustrated. Various test cases are simulated and compared to known solutions.
- **Chapter Five: Fluid-Structure Interaction: Implementation.**
The implementation of the partitioned fluid-structure interaction methodology enabling strong coupling between the structure and the fluid is proposed.
- **Chapter Six: Fluid-Structure Interaction: Results and Evaluation.**
The validity of the FSI scheme is assessed against a test case. Furthermore, results of the FSI scheme applied to a real-life gust case are discussed.
- **Chapter Seven: Conclusion and Recommendations.**
The work completed is summarised and recommendations for the continuation of the work is proposed.

Chapter 2

Structural Model Governing Equations

2.1 Introduction

The aim of this project is to develop a technology that provides a platform to complete aircraft loads calculations with various resolution ROMs. The focus is especially on the strongly-coupled fluid-structure interaction problems that arise as a result of the sloshing loads within a wing fuel tank. In order to complete these objectives, a robust structural model needs to be developed. Therefore, it is essential to derive the set of equations which describe the solid continuum in terms of the Lagrangian configuration. This is done via the fundamental concepts of differential calculus and theory of elasticity. Timoshenko beam assumptions accounting for the rotary inertia and shear deformation effects are also included.

2.2 Timoshenko Beam Theory

The wing structure may be represented by a three-dimensional beam. The simplest beam theory is known as Euler-Bernoulli beam theory (EBBT) and states that plane sections of this beam remain plane and perpendicular to the centroidal axis under deformation [24]. Consequently, this theory ignores stresses due to shear deformation, unlike Timoshenko beam theory (TBT) which includes the shear deformation effects [25]. TBT also includes rotary inertia which is particularly important for composite beam vibrational analysis [26]. It also provides greater approximation of primary natural frequencies, with the EB model deviating in the second natural frequency by up to 50% [27]. Note that for the purposes of this work, linear displacements are assumed as these are deemed appropriate for typical wing flex due to the nature of an aircraft wing.

2.2.1 Problem Formulation

In order to derive the governing equation with respect to the beam displacement, we first consider the quasi-static beam under the influence of a distributed load, $q(x)$, per unit length. The loading condition alters the orientation of the beam in the (x, y, z) -coordinate system, from its undeformed reference position (Fig. 2.1) to a deformed position (Fig. 2.2).

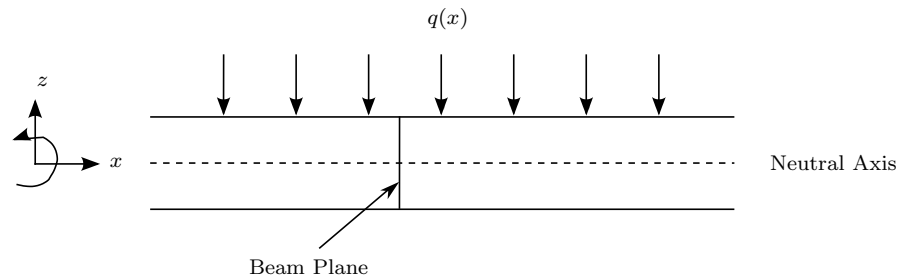


Figure 2.1: Undeformed beam under distributed loading $q(x)$

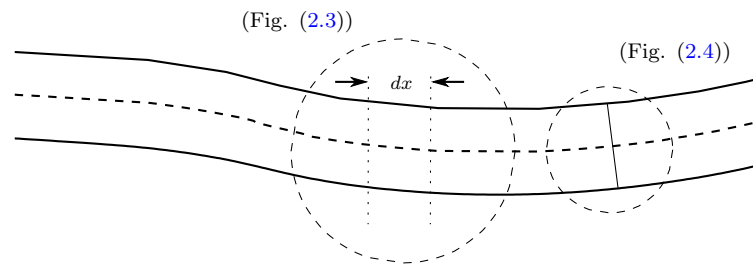


Figure 2.2: Beam in the deformed configuration with differential element, dx , and deformed beam plane

From the differential beam element cross-section (Fig. 2.3) it can be seen that the external loads are balanced by internal section shear forces and moments, V and M . The infinitesimally small part of the beam is initially only considered in two-dimensional space for simplicity and thus placed in the $x-z$ plane. Evaluating the vertical force equilibrium of the differential beam element

$$\sum F_z = 0 \quad (2.1)$$

$$\therefore -V + q(x)dx + V + dV = 0 \quad (2.2)$$

Similar to Eq. (2.2), the moment equilibrium is evaluated by computing the moment around the left edge of the element in a counter clockwise direction.

$$\sum M_y = 0 \quad (2.3)$$

$$\therefore M + q(x)dx \frac{dx}{2} - (M + dM) + (V + dV)dx = 0 \quad (2.4)$$

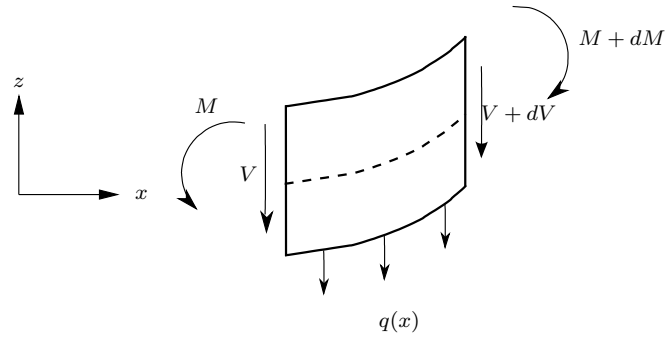


Figure 2.3: Differential free body diagram of the forces and moments acting on the beam

Upon simplification and disregarding the second order terms, the governing equations for the beam may be written as

$$\frac{dV}{dx} + q(x) = 0 \quad (2.5)$$

$$\frac{dM}{dx} - V = 0 \quad (2.6)$$

Combining the above results in the governing equations for the beam produce

$$\frac{d^2M}{dx^2} + q(x) = 0 \quad (2.7)$$

In order to describe the behaviour of the beam from the differential equation of motion above, the kinematics of the beam is introduced. The deformation kinematics of the cross-sectional element, dx , is illustrated in Fig. 2.4. Here $w(x)$ and θ represent the lateral displacement of the neutral axis and the rotation of the cross-section at the mid-plane respectively.

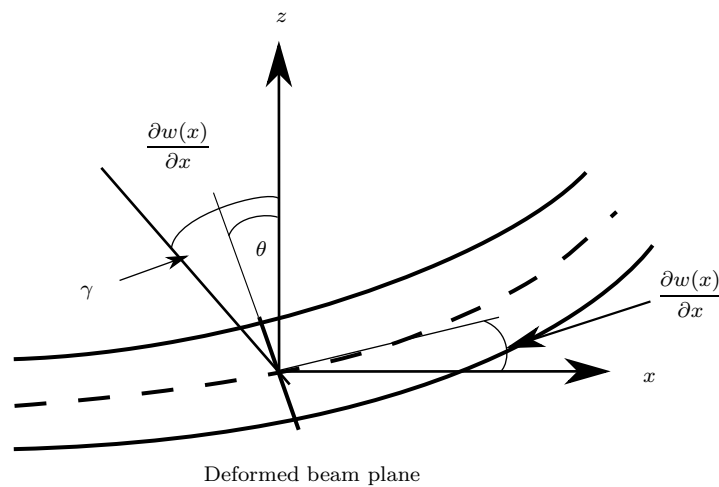


Figure 2.4: Kinematics of the Timoshenko beam

Timoshenko beam cross-sections remain straight after deformation, however they do not remain perpendicular to the neutral axis because of the shear effects. The total deflection of a particle on the beam is due to both bending and shear forces. In turn, this causes the rotation of the cross-section at the mid-plane to be

$$\theta = \frac{\partial w(x)}{\partial x} - \gamma \quad (2.8)$$

where $w(x)$ is the lateral displacement of the neutral axis and γ denotes the induced shear angle. From these kinematic assumptions for a Timoshenko beam the displacements of the beam are given by

$$u_x = -z\theta \quad (2.9)$$

$$u_y = 0 \quad (2.10)$$

$$u_z = w(x) \quad (2.11)$$

From the displacements above, the normal and shear strains may be expressed as follows

$$\varepsilon_{xx} = \frac{\partial u_x}{\partial x} = z \frac{\partial \theta}{\partial x} \quad (2.12)$$

$$\varepsilon_{yy} = \frac{\partial u_y}{\partial x} = 0 \quad (2.13)$$

$$\varepsilon_{xz} = \frac{1}{2} \left(\frac{\partial u_x}{\partial y} + \frac{\partial u_z}{\partial x} \right) = \frac{1}{2} \left(\theta + \frac{\partial w(x)}{\partial x} \right) \quad (2.14)$$

Due to the varying shear strain over the cross-section, a correction factor, κ , is introduced [28]

$$\varepsilon_{xz} = \frac{1}{2} \kappa \left(\theta + \frac{\partial w(x)}{\partial x} \right) \quad (2.15)$$

This coefficient is dependent on Poisson's ratio and represents the ratio of the average shear strain on a section to the shear strain at the centre [29], as follows

$$\int_A \tau dA = \kappa AG\theta \quad (2.16)$$

where τ represents the shear stress, while A and G are the area and shear modulus respectively. In engineering practices, approximations are adequate for general cases, with the shear correction factor for a solid rectangular, κ_R , and circular cross-section, κ_C , respectively as

$$\kappa_R = \frac{10(1 + \nu)}{12 + 11\nu} \quad (2.17)$$

$$\kappa_C = \frac{6(1 + \nu)}{7 + 6\nu} \quad (2.18)$$

where ν denotes Poisson's ratio. The plane stress condition arises when a body

is thin i.e. the third dimension is negligible in relation to the other dimensions. As a result, the 2D beam may be considered a plane stress problem resulting in

$$\sigma_{yy} = \sigma_{xy} = \sigma_{yz} = 0 \quad (2.19)$$

According to the constitutive relationship of the material, the normal and shear strains are related to the associated normal and shear stresses as

$$\sigma_{xx} = E\varepsilon_{xx} = Ez \frac{\partial \theta(x, t)}{\partial x} \quad (2.20)$$

$$\sigma_{xz} = 2G\varepsilon_{xz} = \kappa G \left(\theta + \frac{\partial w(x, t)}{\partial x} \right) \quad (2.21)$$

where E and G represent the elastic and shear moduli respectively. Finally, we employ the theory of elasticity which states that the stresses on an element face should be statically equivalent to the components of the moment and shear force acting upon it as follows [30]

$$M = - \int_A z \sigma_{xx} dA \quad (2.22)$$

$$V = \int_A \sigma_{xz} dA \quad (2.23)$$

From the above, it follows that

$$M = - \int_A z E \varepsilon_{xx} dA = \int_A z^2 E \frac{\partial \theta(x, t)}{\partial x} dA = EI \frac{\partial \theta(x, t)}{\partial x} \quad (2.24)$$

and

$$V = \int_A \sigma_{xz} dA = \int_A 2G \varepsilon_{xz} dA = \int_A \kappa G \left(\theta + \frac{\partial w(x, t)}{\partial x} \right) dA \quad (2.25)$$

$$\therefore V = \kappa AG \left(\theta + \frac{\partial w(x, t)}{\partial x} \right) \quad (2.26)$$

where I is the area moment of inertia and equivalent to $I = \int_A z^2 dA$. Substituting Eqs. (2.5) and (2.6) into (2.24) and (2.26), the coupled governing equations of a Timoshenko beam may be expressed for the rotation balance as

$$\frac{\partial}{\partial x} \left(EI \frac{\partial \theta}{\partial x} \right) + \kappa AG \left(\frac{\partial w(x)}{\partial x} - \theta \right) = 0 \quad (2.27)$$

and force balance

$$\frac{\partial}{\partial x} \left[\kappa AG \left(\frac{\partial w(x)}{\partial x} - \theta \right) \right] + q(x) = 0 \quad (2.28)$$

For a unique solution to the governing equations, appropriate boundary conditions are to be prescribed. These may be in terms of displacements (kinematic boundary condition) or external forces (mechanical boundary condition). For dynamic cases initial conditions are also required.

The above is now extended to the transient (dynamic) case. Similar to the approach of the quasi-static beam derivation, a differential element is considered for force and moment balance. To allow for vibrations, the rotary inertia, $\rho I \frac{\partial^2 \theta}{\partial t^2}$, as well as the acceleration, $\rho A \frac{\partial^2 w(x, t)}{\partial t^2} dx$, of the differential element are included. Here, ρ denotes the density. Following the balance of forces and moments, the dynamic governing equations of a Timoshenko beam can thus be expressed by

$$\frac{\partial}{\partial x} \left(EI \frac{\partial \theta}{\partial x} \right) + \kappa AG \left(\frac{\partial w(x, t)}{\partial x} - \theta \right) - \rho I \frac{\partial^2 \theta}{\partial t^2} = 0 \quad (2.29)$$

$$\frac{\partial}{\partial x} \left[\kappa AG \left(\frac{\partial w(x, t)}{\partial x} - \theta \right) \right] + q(x, t) - \rho A \frac{\partial^2 w(x, t)}{\partial t^2} = 0 \quad (2.30)$$

and the translation and torsional balance reads

$$\frac{\partial}{\partial x} \left[AE \left(\frac{\partial u(x, t)}{\partial x} \right) \right] + b(x, t) = 0 \quad (2.31)$$

$$\frac{\partial}{\partial x} \left[GJ \left(\frac{\partial \phi(x, t)}{\partial x} \right) \right] + T(x, t) = 0 \quad (2.32)$$

where $u(x, t)$ is the axial displacement and $\phi(x, t)$ the angular displacement while the axial and torsional forces are defined as $b(x, t)$ and $T(x, t)$.

2.3 Conclusion

This chapter detailed the equations employed to describe the structural model which forms the platform of loads calculations. Linear dynamic TBT was employed as it describes the vertical displacements and rotations of a typical wing structure with sufficient accuracy under normal operating conditions. The following chapter entails the discretisation and solution procedure to effect the governing equations in a fully coupled manner.

Chapter 3

Structural Model: Numerical Discretisation

3.1 Introduction

As noted in Chapter 2, the aircraft structure is represented by a Timoshenko beam ROM. This chapter involves the development of the numerical solution required to solve the governing equations. This includes both spatial and temporal aspects. The numerical techniques to be described were chosen specifically to ensure both accuracy and robustness.

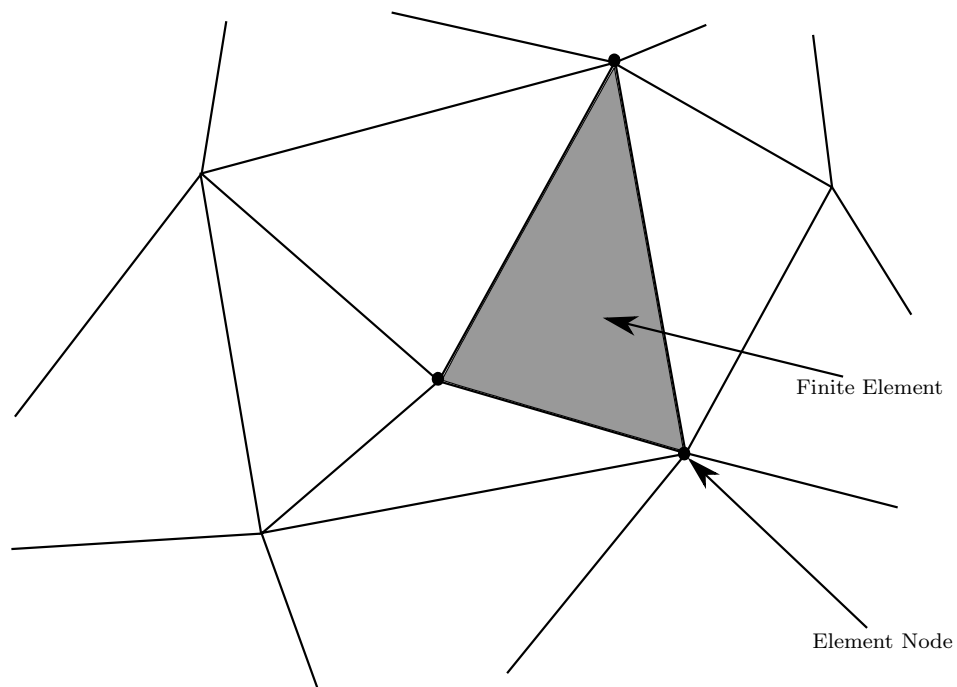


Figure 3.1: Diagram of the finite element method on a 2D unstructured grid

3.2 Finite Element Method

Determining an analytical solution to the governing equations of motion derived previously for the general case provides formidable complexity. This warrants a numerical solution. The finite element method (FEM) has proven itself to be superior when considering slender beam structures [31][32]. The approach involves replacing the actual continuous (physical) structure by a mathematical model comprising of structural elements with a finite size. These elements contain the elastic and inertial properties of the continuum it represents. Furthermore, these element-wise mathematical models are assembled appropriately to form an overall mass and stiffness matrix from which the beam static and dynamic response may be computed when subjected to specified loads.

In this chapter, the principle of virtual work is the basic relationship used for the finite element formulation to relate external work with internal work. This principle states that the equilibrium of the body requires that the total internal virtual work is equal to the total external virtual work [33], as follows

$$\delta W_i = \delta U_i \quad (3.1)$$

where W_i and U_i respectively denote external and internal work in Cartesian coordinate direction i . This means that the stresses induced in a body should be in equilibrium with any externally applied loads, as follows

$$\int_V \epsilon \tau dV = \int_V \mathbf{u} f_b dV + \int_S \mathbf{u} f_s dS + \sum \mathbf{u} R_c \quad (3.2)$$

where ϵ are the virtual strains, τ represents the stresses induced in the body and \mathbf{u} is the virtual displacements experienced within an element. The externally applied loads may be represented by R_c , f_b and f_s which correspond to possible point loads, body forces and surface forces respectively. Further, \int_V and \int_S denote the integral over an element volume and bounding surface respectively. In deriving the finite element formulation, this virtual relationship is utilised to discretise the solid continuum into discrete algebraic equations.

3.3 Spatial Discretisation

This section will firstly detail the process involved in applying the finite element formulation to a general three-dimensional body (Fig. 3.2). Subsequently, it will be specialised to find the governing equations of the Timoshenko beam under consideration. As pointed out previously, we commence by discretising the domain into finite non-overlapping elements. Elements are mathematically connected via vertexes or nodes. We assume the displacements within an element i.e. between nodes, to be a function of the nodal displacements. Therefore an interpolation scheme is used to determine the relationship between the nodal displacements and the element internal displacements. The choice and construction of an appropriate interpolation scheme will be discussed later.

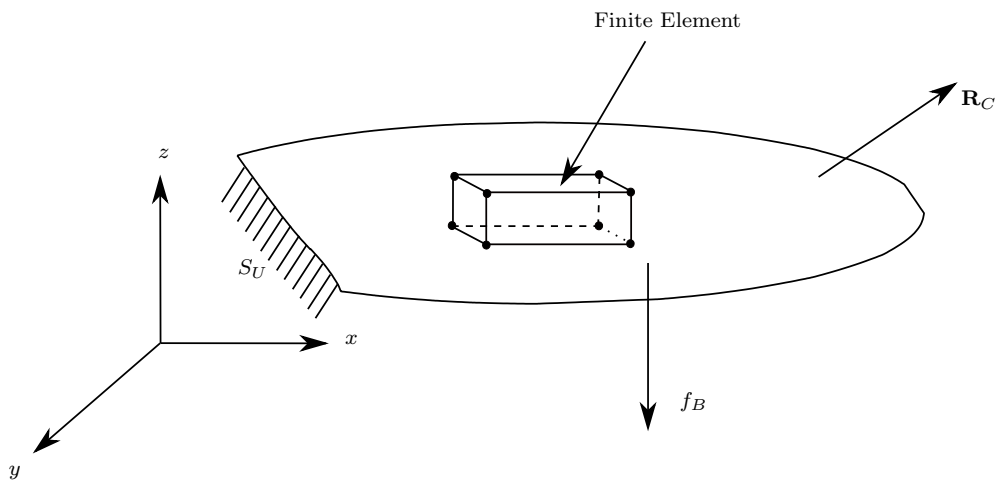


Figure 3.2: Diagram of a general continuum body under loading

Considering an element, e , we introduce the interpolation relationship for displacement within the element, \mathbf{u}_e , as

$$\mathbf{u}_e = \mathbf{N} \{\mathbf{U}\} \quad (3.3)$$

where \mathbf{N} is the displacement interpolation matrix and $\{\mathbf{U}\}$ is the vector of nodal displacements and/or rotations. The relationship is extended to evaluate the strain within each element as follows

$$\epsilon = \mathbf{B} \{\mathbf{U}\} \quad (3.4)$$

where \mathbf{B} represents the strain-displacement relationship by differentiating the rows of \mathbf{N} appropriately i.e.

$$\mathbf{B} = \frac{d\mathbf{N}}{dx} \quad (3.5)$$

In order to complete the principle of virtual work (Eq. (3.2)), the stresses within each finite element are also required. These stresses are related to the strains by the constitutive relationship.

$$\tau_e = \mathbf{C}_e \epsilon_e \quad (3.6)$$

where \mathbf{C}_e is the elasticity matrix of the element e and contains the material information of the element. A linear relationship between the stress and the strain may be assumed due to small deformations and thus infinitesimal strains experienced by the body. Using the above relations, it is possible to discretise the virtual work equilibrium equations in an element-wise manner as

$$\sum_e \int_V \epsilon \tau dV = \sum_e \int_V \mathbf{u}_e f_b dV + \sum_e \int_S \mathbf{u}_e f_s dS + \sum \mathbf{u}_e R_c \quad (3.7)$$

where $e = 1, 2, \dots, m$, and m is the total number of elements in the structure. The shape functions, described by Eq. (3.3), and subsequent constitutive relationships (Eqs. (3.4) and (3.6)) are incorporated into the principle of virtual displacements (Eq. (3.7)) to obtain the discrete equations

$$\mathbf{U}^T \left[\sum_e \int_V \mathbf{B}^T \mathbf{C}_e \mathbf{B} dV_e \right] \mathbf{U} = \mathbf{U}^T \left[\left\{ \sum_e \int_V \mathbf{N} \mathbf{f}_e^B dV_e \right\} + \left\{ \sum_e \int_S \mathbf{N} \mathbf{f}_e^S dS_e \right\} + \mathbf{R}_C \right] \quad (3.8)$$

using the nomenclature described previously. The nodal displacement vector, \mathbf{U} , may be removed from the integral as it contains constant nodal values. The various matrices may now be established from the above relationship. The stiffness matrix of the structure, \mathbf{K} , is the assembled matrix of all the element stiffnesses as follows

$$\mathbf{K} = \sum_e \int_V \mathbf{B}^T \mathbf{C}_e \mathbf{B} dV_e \quad (3.9)$$

We now define the load vector, \mathbf{R} , comprising of the element body forces, \mathbf{R}^B , the effect of element surface forces, \mathbf{R}^S and the nodal concentrated loads, \mathbf{R}^C ,

$$\mathbf{R} = \mathbf{R}^B + \mathbf{R}^S + \mathbf{R}^C \quad (3.10)$$

where

$$\mathbf{R}^B = \sum_e \int_V \mathbf{N}^T \mathbf{f}_e^B dV_e \quad (3.11)$$

$$\mathbf{R}^S = \sum_e \int_S \mathbf{N}^T \mathbf{f}_e^S dS_e \quad (3.12)$$

from which the final set of discrete equations describing the mechanics of the structure results

$$\mathbf{K}\mathbf{U} = \mathbf{R} \quad (3.13)$$

This may be extended to encompass the dynamic as well as viscous damping effects as

$$\mathbf{M}\ddot{\mathbf{U}} + \mathbf{C}\dot{\mathbf{U}} + \mathbf{K}\mathbf{U} = \mathbf{R} \quad (3.14)$$

where the mass matrix of the structure is

$$\mathbf{M} = \sum_e \int_V \rho_e \mathbf{N}^T \mathbf{N} dV_e \quad (3.15)$$

and \mathbf{C} , $\dot{\mathbf{U}}$ and $\ddot{\mathbf{U}}$ are respectively the viscous damping matrix, nodal velocity and acceleration vectors.

3.3.1 Spatial discretisation of the Timoshenko beam

With regards to the Timoshenko beam, the principle of virtual displacements is applied to the governing equations due to bending, axial and torsional deformation. These are re-stated for the sake of convenience

$$\begin{aligned} \frac{\partial}{\partial x} \left(EI \frac{\partial \theta}{\partial x} \right) + \kappa AG \left(\frac{\partial w(x, t)}{\partial x} - \theta \right) - \rho I \frac{\partial^2 \theta}{\partial t^2} &= 0 \\ \frac{\partial}{\partial x} \left[\kappa AG \left(\frac{\partial w(x, t)}{\partial x} - \theta \right) \right] + q(x, t) - \rho A \frac{\partial^2 w(x, t)}{\partial t^2} &= 0 \\ \frac{\partial}{\partial x} \left[AE \left(\frac{\partial u(x, t)}{\partial x} \right) \right] + b(x, t) &= 0 \\ \frac{\partial}{\partial x} \left[GJ \left(\frac{\partial \phi(x, t)}{\partial x} \right) \right] + T(x, t) &= 0 \end{aligned}$$

which are discretised using the beam element shown in Fig. 3.3. The resulting displacement in the z -direction due to bending reads

$$\begin{aligned} &\left[\rho I \int_0^L \mathbf{N}^T \mathbf{N} dx + EI \int_0^L \left(\frac{d\mathbf{N}}{dx} \right)^T \left(\frac{d\mathbf{N}}{dx} \right) dx \right. \\ &\left. + \kappa GA \int_0^L \left(\frac{d\mathbf{N}}{dx} + \mathbf{N} \right)^T \left(\frac{d\mathbf{N}}{dx} + \mathbf{N} \right) dx \right] \mathbf{U} = \mathbf{R}_b \end{aligned} \quad (3.16)$$

while axial tension produces x -displacements as

$$\left[AE \int_0^L \left(\frac{d\mathbf{N}}{dx} \right)^T \left(\frac{d\mathbf{N}}{dx} \right) dx \right] \mathbf{U} = \mathbf{R}_a \quad (3.17)$$

Finally, rotational (torsional) displacements are computed from

$$\left[GJ \int_0^L \left(\frac{d\mathbf{N}}{dx} \right)^T \left(\frac{d\mathbf{N}}{dx} \right) dx \right] \mathbf{U} = \mathbf{R}_t \quad (3.18)$$

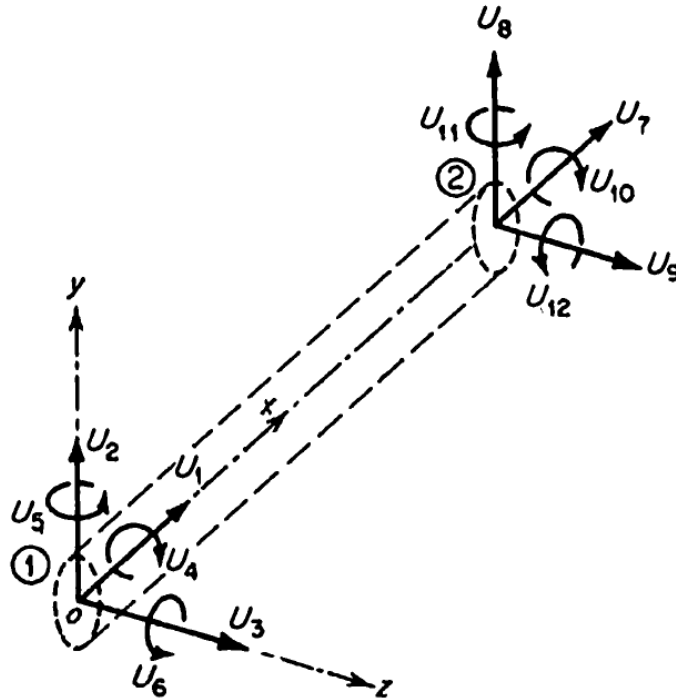


Figure 3.3: Diagram of the beam element with 12 degrees-of-freedom per element [31]

The choice of shape functions for each mode of deflection is considered next. Firstly, the axial and torsional deformations are described via a linear interpolation method due to their linear response to force [34].

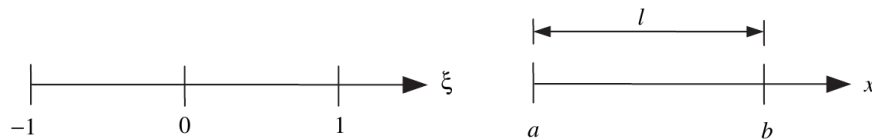


Figure 3.4: Mapping of a 1D domain from the physical domain $[a, b]$ to the parent domain $[-1, 1]$ [35]

For this purpose, we introduce natural coordinates to allow for easier mathematical integration of the shape functions. It may be regarded as a transformation from the physical domain to the natural domain where numerical integration takes

place. Consequently, the shape function is represented as a function of ξ , with ξ only existing between ± 1 i.e.

$$N_a = f(\xi) \quad , \quad -1 \leq \xi \leq 1 \quad , \quad \xi \in \mathbb{R} \quad (3.19)$$

$$N_a = N_t = \left[\frac{1}{2}(1 - \xi) \quad \frac{1}{2}(1 + \xi) \right] \quad (3.20)$$

where N_a and N_t correspond to the axial and torsional shape functions. Due to the more complex (higher order) nature of bending, Hermitian shape functions are employed as

$$\begin{aligned} N_{w1} &= \frac{1}{4}(1 - \xi)^2(2 + \xi) & N_{w2} &= \frac{1}{4}(1 + \xi)^2(2 - \xi) \\ N_{\theta1} &= \frac{l}{8}(1 - \xi)^2(1 + \xi) & N_{\theta2} &= \frac{l}{8}(1 + \xi)^2(1 - \xi) \end{aligned} \quad (3.21)$$

where w_1 and w_2 respectively denote the transverse displacements at each node and θ is the corresponding angular displacement at each node. These shape functions are utilised due to the transverse displacement of the beam being caused by both the nodal displacements as well as the nodal rotations. They may also be derived intuitively from the fact that any shape function, N_i , should be 1 at the degree-of-freedom (dof) under consideration and 0 at every other dof. The displacement and rotation in a two-dimensional plane may now be expressed as

$$\begin{pmatrix} w(x) \\ \theta \end{pmatrix} = \begin{bmatrix} N_{w1} & 0 & N_{w2} & 0 \\ 0 & N_{\theta1} & 0 & N_{\theta2} \end{bmatrix} \begin{Bmatrix} w_1(x) \\ \theta_1 \\ w_2(x) \\ \theta_2 \end{Bmatrix} \quad (3.22)$$

$$\mathbf{u} = \mathbf{N} \{\mathbf{U}\} \quad (3.23)$$

To complete the discretisation of the governing equation (Eq. (3.16)), we consider the strain matrix \mathbf{B} . This involves the derivatives of the shape functions with respect to the physical coordinates x . An isoparametric formulation is employed (same shape function as used for the displacements)

$$\mathbf{x} = \mathbf{N} \{x\} \quad (3.24)$$

From the chain rule the strain matrix may be found to be

$$\frac{\partial N_i}{\partial \xi} = \frac{\partial N_i}{\partial \mathbf{x}_1} \frac{\partial \mathbf{x}_1}{\partial \xi} + \frac{\partial N_i}{\partial \mathbf{x}_2} \frac{\partial \mathbf{x}_2}{\partial \xi} \quad (3.25)$$

The discretisation may now be completed for the Timoshenko beam (Fig. 3.3), consisting of 12 degrees of freedom. Each element consists of 2 nodes which have 6 dofs per node. Upon substitution of the shape functions and integration of Eqs. 3.16, 3.17 and 3.18, the governing equations may be cast in matrix form. For a

uniform beam element with symmetrical cross-section the element stiffness, $[\mathbf{K}]_e$, and mass matrix, $[\mathbf{M}]_e$, can be found explicitly by performing an analytical integration. Further, the shape functions are under-integrated to avoid shear locking and produce the element stiffness and mass matrices as listed in Appendix A.

These element stiffness and mass matrices are assembled to form the overall matrices. The assembly process assigns the local element dof to the global dof resulting in a square stiffness and mass matrix of size n , where n is the number of global dofs. The beam elements constituting the structure are linked end-to-end with adjacent elements contributing to the connecting node. The principle of superposition enables these elements to donate their respective stiffness and mass values to the adjoining node's global dofs.

3.3.2 Boundary Conditions and Loading

To achieve a unique solution, appropriate essential and natural boundary conditions (BCs) are to be applied. The former involve displacements, while the latter is concerned with forces. As this study focused on a wing beam, which is supported at its base, the essential condition applied involved constraining all displacements at the root. The force boundary condition involved point, distributed and slosh related forces.

3.4 Temporal Discretisation

Temporal discretisation is effected via the Newmark method, which was selected due its accuracy and robustness. The frequency domain solution on the other hand involved solving the eigen-problem. The aforementioned is considered first.

3.4.1 Newmark Method

To recap, the dynamic equilibrium equations of motion are

$$\mathbf{M}\ddot{\mathbf{U}} + \mathbf{C}\dot{\mathbf{U}} + \mathbf{K}\mathbf{U} = \mathbf{R} \quad (3.26)$$

where \mathbf{M} , \mathbf{C} and \mathbf{K} are respectively the mass, damping and stiffness matrices. Further, \mathbf{U} denotes the 6 degrees-of-freedom to be solved for at each node (three rotations and three translations in 3D), with single and double dot quantities denoting velocity and acceleration respectively.

The Newmark method is a popular direct integration method due to its desirable accuracy and stability characteristics. The procedure involves computing velocities and displacements at the next time step via the following expressions

$$\dot{\mathbf{U}}^{t+\Delta t} = \dot{\mathbf{U}}^t + \Delta t \left[(1 - \delta)\ddot{\mathbf{U}}^t + \delta\ddot{\mathbf{U}}^{t+\Delta t} \right] \quad (3.27)$$

$$\mathbf{U}^{t+\Delta t} = \mathbf{U}^t + \Delta t\dot{\mathbf{U}}^t + \Delta t^2 \left[\left(\frac{1}{2} - \alpha\right)\ddot{\mathbf{U}}^t + \alpha\ddot{\mathbf{U}}^{t+\Delta t} \right] \quad (3.28)$$

where α and δ are stability parameters. The method is implicit and conditional stability is guaranteed when

$$\delta \geq \frac{1}{2} \text{ and } \alpha \geq \frac{1}{4} \left(\delta + \frac{1}{2} \right)^2 \quad (3.29)$$

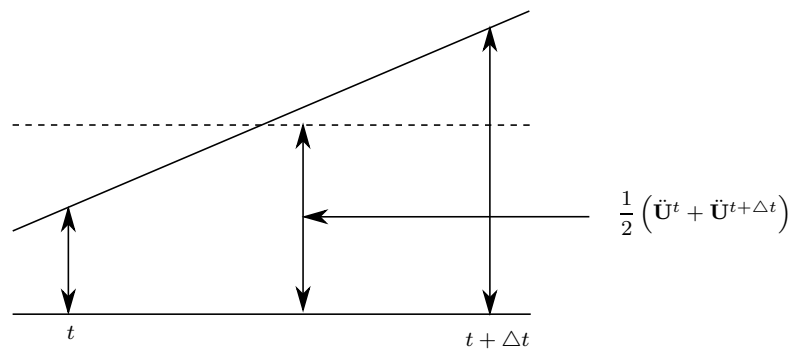


Figure 3.5: Newmark's constant-average-acceleration scheme [33]

with the preferred choice being $\alpha = 1/4$ and $\delta = 1/2$ on grounds of robustness and enforcement of second-order accuracy. Acceleration and velocity at the next

time step may then be computed from the unknown displacements at the next time step $\mathbf{U}^{t+\Delta t}$ by

$$\ddot{\mathbf{U}}^{t+\Delta t} = \frac{1}{\alpha\Delta t^2}(\mathbf{U}^{t+\Delta t} - \mathbf{U}^t) - \frac{1}{\alpha\Delta t}\dot{\mathbf{U}}^t - \left(1 - \frac{1}{2\alpha}\right)\ddot{\mathbf{U}}^t \quad (3.30)$$

$$\dot{\mathbf{U}}^{t+\Delta t} = \frac{\delta}{\alpha\Delta t}(\mathbf{U}^{t+\Delta t} - \mathbf{U}^t) - \left(\frac{\delta}{\alpha} - 1\right)\dot{\mathbf{U}}^t - \left(\frac{\delta}{2\alpha} - 1\right)\Delta t\ddot{\mathbf{U}}^t \quad (3.31)$$

Applying the above to the equations of motion results in a set of algebraic equations with the future displacement as the only unknown, which may be computed by means of a linear solver. A critical consideration is the size of the time step. Stability is ensured if the time step is small enough to integrate accurately the response of the highest frequency component [36]. An approximation to an appropriate time step may be $\Delta t = \frac{T_p}{20}$, where $T_p = 2\pi/\omega_{co}$ and ω_{co} corresponds to the highest frequency that might be experienced by the structure. For the purpose of this work, ω_{co} is taken as the fifth mode and is computed via eigen-value analysis. With regards to accuracy, this does not induce any numerical damping and preserves energy.

3.4.2 Modal Analysis

Modal analysis via numerical methods is a powerful tool that provides key dynamic properties of a structure caused by vibration. In addition, it allows faster computation of the dynamic response as compared to the method outlined above. In order to determine the natural frequencies and mode shapes, also known as the eigen-values and eigen-vectors, it is required to solve the eigen-problem of the structure. The generalised eigen-problem without the effects of damping may be described by

$$\mathbf{K}\phi = \omega^2\mathbf{M}\phi \quad (3.32)$$

where ϕ is an eigen-vector and ω represents the frequency of vibration in $rad.s^{-1}$. Also, \mathbf{M} and \mathbf{K} serve as the system mass and stiffness matrices respectively (which are computed as outlined in the previous section). The eigen-problem presents n paired eigen-solutions, where n is the number of degrees of freedom of the problem. As a result, we can write the solutions as

$$\mathbf{K}\Phi = \mathbf{M}\Phi\Omega^2 \quad (3.33)$$

where Φ defines a matrix whose columns are the eigen-vectors, ϕ_i and Ω^2 is a diagonal matrix which contains the eigen-values ω_i^2 . The eigen-vectors are mass ortho-normalised which results in the identity matrix, of size n , when multiplied with the mass matrix as

$$\Phi^T\mathbf{M}\Phi = [\mathbf{I}]; \quad \Phi^T\mathbf{K}\Phi = [\Omega^2] \quad (3.34)$$

This leads to the following transformed equation of motion that correspond to the modal generalised displacements

$$\ddot{\mathbf{X}}(t) + \mathbf{\Omega}^2 \mathbf{X}(t) = \mathbf{\Phi}^T \mathbf{R}(t) \quad (3.35)$$

where $\ddot{\mathbf{X}}$ and \mathbf{R} are respectively the accelerations and the residual matrix. As pointed out previously, the above allows for efficient computation of the dynamic response of the system. Therefore, once the eigen-vectors and eigen-values are calculated (Eq. (3.32)), the dynamic solution may be found in the frequency domain at a significantly reduced cost. The Newmark integration scheme may again be employed for the purpose of stable and accurate time integration. In passing, the reader is reminded that the eigen-solution is also required for the computation of damping to ensure an accurate and stable time-domain solution.

Due to the nature of the eigen-problem it will be required to deal with large, sparse and symmetric matrices. A matrix is considered large when its dimension, n , extends to over hundreds of thousands in size. Moreover, the matrix will be considered sparse when it contains few non-zero entries, as can be seen in an example of a matrix matrix under consideration.

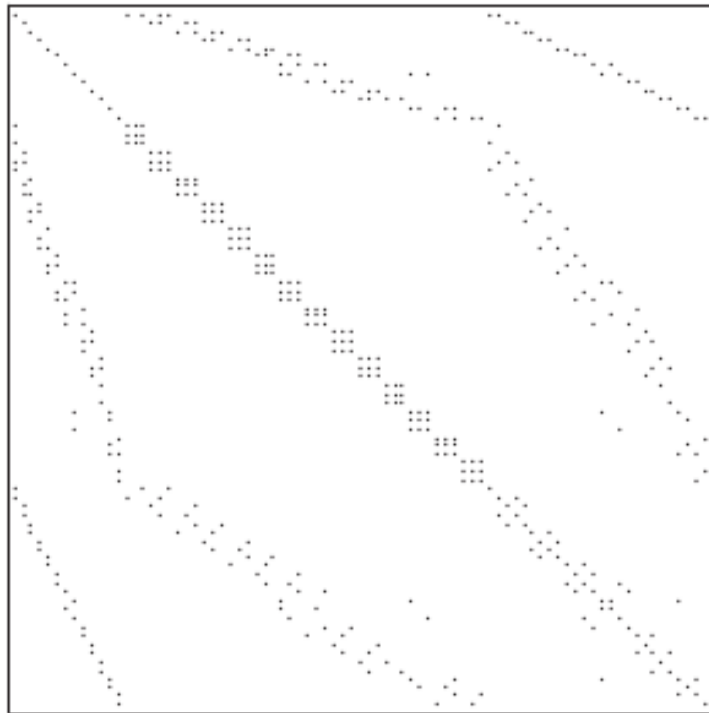


Figure 3.6: Illustration of a sparse, symmetric matrix with few non-zero values shown

Even though the generalised eigen-problem is of primary concern during structural analysis, the standard eigen-problem is the simplest. The standard eigen-problem evaluates one matrix, \mathbf{D} , as

$$\mathbf{D}\phi = \lambda\phi \quad (3.36)$$

where λ is the eigen-value that corresponds to the natural frequency squared, ω_i^2 , while ϕ remains the eigen-vector. The following sections will detail the procedure to firstly reduce the generalised eigen-problem to the standard eigen-problem. From there the Arnoldi method will be introduced to decrease the complexity of the problem. Lastly, Gram-Schmidt decomposition is introduced from which the eigen-vectors and eigen-values may be determined.

3.4.2.1 Cholesky Factorisation

In order to resolve the eigen-problem it is essential to first reduce the generalised eigen-problem (Eq. (3.32)) to a similar standard eigen-problem (Eq. (3.36)). This is done by performing a Cholesky factorisation on the mass matrix, as follows

$$\mathbf{M} = \mathbf{L}\mathbf{L}^T \quad (3.37)$$

where \mathbf{L} is the lower triangular matrix and \mathbf{L}^T representing its transpose, which is an upper triangular matrix. By substituting Eq. (3.37) into (3.32) we obtain

$$\mathbf{K}\phi = \lambda\mathbf{L}\mathbf{L}^T\phi \quad (3.38)$$

By determining the inverse of the triangular matrices along with matrix manipulation and substitution, the conversion to the standard eigen-problem may be found as follows

$$\mathbf{L}^{-1}\mathbf{K}\phi = \lambda\mathbf{L}^T\phi, \quad \text{Let } \mathbf{L}^T\phi = y, \quad (3.39)$$

$$\therefore \mathbf{L}^{-1}\mathbf{K}\mathbf{L}^{-T}y = \lambda y \quad (3.40)$$

$$\therefore \mathbf{D}y = \lambda y \quad (3.41)$$

where $\mathbf{D} = \mathbf{L}^{-1}\mathbf{K}\mathbf{L}^{-T}$. Moreover, a transformation was performed which renders y the transformed eigen-vector. To obtain the eigen-vectors in the original coordinates, ϕ , Eq. (3.39) is employed. In the section to follow, we consider reducing the order of the problem to be solved.

3.4.2.2 Arnoldi Method

The Arnoldi method builds an orthogonal basis of the Krylov subspace, which is the subspace of orthogonal vectors spanned by the iterates of the simple Power method [37]. It was developed to reduce a dense matrix into a Hessenberg matrix or more practically, allow for convergence of the Power method onto more than

one eigen-value. The Power method is an iterative process whereby the next approximation to the largest eigen-vector is found by multiplying the previous vector product with the matrix continuously e.g.

$$v = Av = A^2v = \dots = A^{m-1}v \quad (3.42)$$

The basic Arnoldi method reduces the square matrix to an orthogonal upper-Hessenberg matrix of order m , with $m \ll n$. This simpler form of the matrix can be used to find approximations to the dominant eigen-pairs of the initial square matrix. The form of the similarity transform becomes

$$AV_m = V_m H_m \quad (3.43)$$

where $V_m = [v_1, \dots, v_m]$ is a set of orthonormal vectors and H_m is an upper Hessenberg matrix. The Hessenberg matrix contains the primary eigen-pairs to the original, dense matrix. Accordingly, the calculation of eigen-pairs for the reduced Hessenberg matrix, H_m , is much simpler than the overall matrix, A . The Hessenberg matrix contains

$$\begin{pmatrix} x & x & x & x & x \\ x & x & x & x & x \\ 0 & x & x & x & x \\ 0 & 0 & x & x & x \\ 0 & 0 & 0 & x & x \end{pmatrix} \quad (3.44)$$

Figure 3.7: Upper Hessenberg matrix structure

The Arnoldi method to build the Krylov set of vectors and upper Hessenberg matrix is as follows:

Algorithm 1: Arnoldi Method

- 1 **Start:** Choose a vector v_1 of norm 1.
- 2 **Iterate:** for $j = 1, 2, \dots, m$ compute:

$$h_{ij} = (Av_j, v_j), \quad i = 1, 2, \dots, j \quad (3.45)$$

$$w_j = Av_j - \sum_{i=1}^j h_{ij}v_i \quad (3.46)$$

$$h_{j+1,j} = \|w\|_2, \quad \text{if } h_{j+1,j} = 0 \text{ stop} \quad (3.47)$$

$$v_{j+1} = \frac{w_j}{h_{j+1,j}} \quad (3.48)$$

This algorithm thus constructs a reduced upper Hessenberg matrix containing the same eigen-values as the large sparse matrix. As a result, the eigen-pairs are

solved for the Hessenberg matrix via simple eigen-value approximations such as the Gram-Schmidt Decomposition process. The latter method is outlined next.

3.4.2.3 Modified Gram-Schmidt Decomposition

The Gram-Schmidt process is also known as the QR-algorithm as it decomposes a matrix under consideration, \mathbf{H} , as follows

$$\mathbf{H} = QR \quad (3.49)$$

where, Q is a matrix of orthogonal vectors and R is an upper triangular matrix. The modified Gram-Schmidt decomposition is the process involved in breaking down the input matrix into the aforementioned matrices. However, to compute the approximate eigen-values, λ_i , multiple decompositions are required. It is shown that through consecutive decompositions and subsequent product of the decomposed matrices, in reverse order, the approximate eigen-values of the matrix will align along the diagonal.

$$D = QR; R * Q = D; \text{ until } D \text{ is a diagonal matrix} \quad (3.50)$$

Upon computing the approximate eigen-vector of the Hessenberg matrix, \mathbf{H} , associated with the eigen-value, it is necessary to reverse the transformation that occurred during the Arnoldi algorithm. Mathematically, this may be defined as

$$u_i = V_m y_i \quad (3.51)$$

where y_i is an eigen-vector of \mathbf{H} associated with the same eigen-value and V_m represents the Krylov subspace of orthogonal vectors formed during the Arnoldi method. In summary, the solution procedure to the generalised eigen-problem of large, sparse matrices has been developed. There exists various ways to improve the performance of the methods derived above. For the purpose of this project however, the aforementioned theorems are sufficient to provide an accurate result.

3.4.3 Damping Model

Damping is the dissipation of energy from a vibrating structure wherein mechanical energy is typically converted to heat energy. For the analysis of the structure concerned, these dissipative forces need to be considered. The types of damping will vary according to physical properties of the structure. Various models exist to estimate the damping in single degree-of-freedom (SDOF) problems and continuous systems [38][39]. For SDOF, accurate damping models have been found while experimental and hysteretic damping models provide accurate solutions to continuous systems experiencing damping [40].

However for the purposes of this work, a multi degree of freedom (MDOF) damping model is required, of which the viscous variant is popular. This assumes

a linear relationship between the damping force and the velocity

$$F_D = -c\dot{x} \quad (3.52)$$

where F_D , c and \dot{x} is the damping force, velocity and damping coefficient respectively. A subset of viscous damping, Rayleigh proportional damping, is particularly suitable. This is as it expresses the damping matrix, C , as a linear combination of the mass and stiffness matrices

$$\mathbf{C} = \alpha\mathbf{M} + \beta\mathbf{K} \quad (3.53)$$

where α and β are real scalar values. The benefit of this approximation is that it maintains the ability to use modal analysis. Proportional damping assumes that the eigen-vectors, ϕ_i , are also \mathbf{C} -orthogonal, in which case

$$\phi_i^T \mathbf{C} \phi_j = 2\omega_i \zeta_i \delta_{ij} \quad (3.54)$$

where ζ_i is a modal damping ratio and δ_{ij} is the Kronecker delta which exhibits the following properties

$$\delta_{ij} = 1 \quad , \quad \text{for } i = j \quad (3.55)$$

$$\delta_{ij} = 0 \quad , \quad \text{for } i \neq j \quad (3.56)$$

Resultantly, no changes are made to the mode shapes and thus the dynamic response calculation is simplified. In turn this will reduce the system to a set of SDOF differential equations. To determine the damping matrix, we first need the scalar values illustrated in Eq. (3.53). By substituting Eq. (3.53) into (3.54) and using the Kronecker delta property we find

$$\phi_i^T (\alpha\mathbf{M} + \beta\mathbf{K}) \phi_j = 2\omega_i \zeta_i \delta_{ij} \quad (3.57)$$

which may be written as

$$\alpha + \beta\omega_i^2 = 2\omega_i \zeta_i \quad (3.58)$$

$$\therefore \zeta_i = \frac{\alpha}{2} \frac{1}{\omega_i} + \frac{\beta}{2} \omega_i \quad (3.59)$$

The scalar coefficients α and β can now be determined from the specified modal damping ratios ζ_1 and ζ_2 , which correspond to the first and second modes respectively. As stated previously, damping is a phenomenon which should be applied so as to describe the physics specific to a particular structure. Taking cognisance of this and due to an aircraft wing only vibrating within the first 5 modes, a minimum damping of 2% is required, thus $\zeta_1 = \zeta_2 = 0.02$.

$$\frac{1}{2} \begin{bmatrix} 1/\omega_1 & \omega_1 \\ 1/\omega_2 & \omega_2 \end{bmatrix} \begin{Bmatrix} \alpha \\ \beta \end{Bmatrix} = \begin{Bmatrix} \zeta_1 \\ \zeta_2 \end{Bmatrix} \quad (3.60)$$

After determining the scalar coefficients the damping matrix may be calculated and incorporated with ease into the finite element model. This concludes the derivation of the discretisation of the dynamic system in both time and frequency domain.

3.5 Conclusion

In this chapter the finite element method was detailed in order to solve the governing equations of the structure. They were discretised spatially with a Timoshenko beam element that allowed 6 degrees-of-freedom per node, allowing for accurate modelling of typical aircraft wing dynamics. The temporal discretisation was then discussed for the time and frequency domain. With regards to the latter, eigenanalysis procedures for large, sparse systems were illustrated. Damping of the structure was also detailed, to allow inclusion into both temporal and frequency domains. The accuracy of the schemes developed is evaluated for various test problems in the following chapter.

Chapter 4

Structural Model: Verification and Validation

4.1 Introduction

The previous chapter detailed the mathematical description and discretisation method for the wing structural ROM. To assess its accuracy, a validation and verification process is now documented. Both the developed time and frequency domain technology are considered. Additionally, their suitability for use in the aircraft loads calculation under non-linear slosh conditions is assessed.

4.2 Static Bending

The first test case considered was the static response of a 2D cantilever beam under transverse loading, as depicted in Fig. 4.1. The cantilever was investigated due to its analogous behaviour to an aircraft wing with one end being clamped while the free end experiences the load. An isotropic, homogeneous beam was examined with the beam material properties being $E = 71GPa$, $\nu = 0.33$, $\rho = 2586 kg/m^3$, where the variables represent the Young's modulus, Poisson's ratio and density of the beam. Moreover, the beam has an inertia of $I = 2.78 \times 10^{-5} m^4$, second moment of area of $J = 2.09 \times 10^{-5} m^4$, cross-sectional area of $A = 5.6 \times 10^{-5} m^2$ and a length of $l = 5 m$.

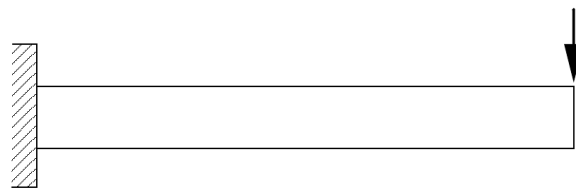


Figure 4.1: Cantilever beam under transverse load

The computational mesh consisted of only 10 elements, and the solution compared to the analytical solution

$$w(x) = \frac{Fx}{\kappa GA} + \frac{F \left(L^2 x - \frac{x^3}{3} \right)}{2EI} - \frac{FL^3}{3EI} - \frac{FL}{\kappa GA} \quad (4.1)$$

where $w(x)$ is the analytical transverse displacement and x is the distance from the cantilever root. Note that the analytical solutions of maximum displacement for a cantilever, y_C , under transverse load may be described as follows [41]:

$$y_C = -\frac{FL^3}{3EI} \quad (4.2)$$

where F is the transverse loading enforced at the beam tip and centre for the cantilever and the simply-supported respectively. The elastic modulus and inertia of the beam is represented by E and I . The predicted displacement is compared to the analytical solution in Fig. 4.2. As shown, the exact solution is replicated accurately. The mesh sizes were also varied to assess mesh independence, and found to have no effect on accuracy. The ROM exhibits a 3^{rd} -order spatial accuracy due to the use of cubic Hermitian shape functions.

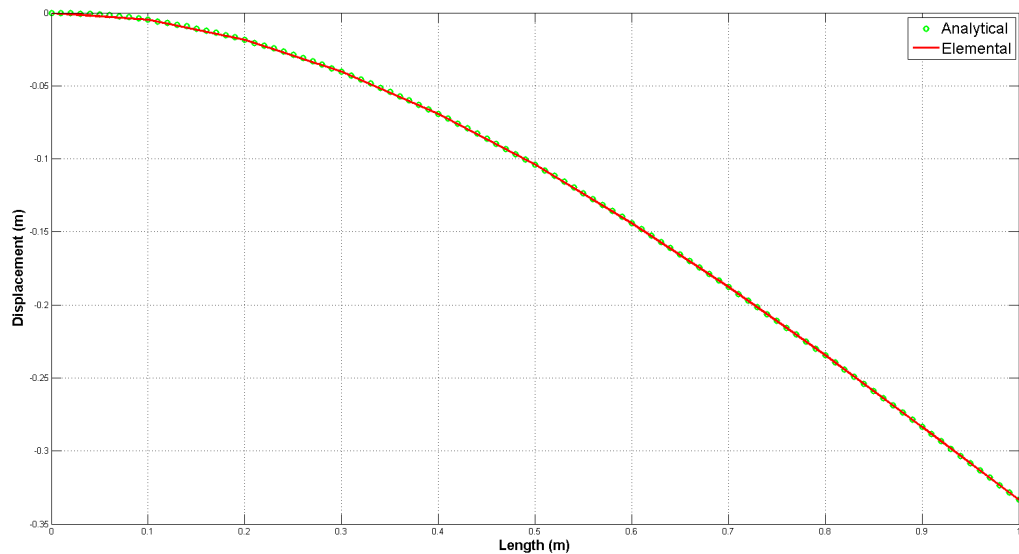


Figure 4.2: Static deformation of a cantilever beam under transverse tip loading

4.3 2D Dynamic Beam

In order to determine the temporal accuracy, a 2D dynamic beam test case was considered, as shown in Fig. 4.3. A cantilever beam, clamped at one end, is subjected to a sudden shear traction at the free end. Analytical solutions only exist for this case when small displacements are experienced and was consequently considered.



Figure 4.3: Cantilever beam under applied shear

The beam has a Young's modulus $E = 0.2$ MPa, Poisson's ratio $\nu = 0.49$, density $\rho = 2000$, length $l = 40$ mm and a cross-section of 0.6 mm \times 10 mm. A shear traction of $\tau = 0.1$ Pa is applied at the free end at time $t = 0$. The analytical solution, in the small displacements limit, is a sinusoidal oscillation [42] defined by

$$u = \frac{4\tau}{E} \frac{l^3}{h^2} (1 - \nu^2) \left[1 + \frac{3}{4}(1 + \nu) \frac{h^2}{l^2} [\cos(\omega_1 t) - 1] \right] \quad (4.3)$$

where ω_1 represents the first natural frequency of oscillation as

$$\omega_1 = \lambda_1^2 \sqrt{\frac{E}{12\rho} \frac{h}{l^2}} \quad (4.4)$$

and λ_1 is the eigen-value of the first mode of oscillation, which for this case is $\lambda_1 = 1.875$. The computed dynamic response shows an accurate correlation compared to the analytical solution, as depicted in Fig. 4.4. Additionally, it was compared to the commercial software developed by NASA, MSC Nastran, and found to yield almost identical results. The l_2 norm of the difference between the Elemental and analytical solutions is 5%, and is ascribed to the latter only accounting for one mode. The numerical solutions is therefore deemed the more accurate. The Newmark employed ensures 2^{nd} -order. As such only 10 elements was deemed accurate enough to assess the temporal accuracy.

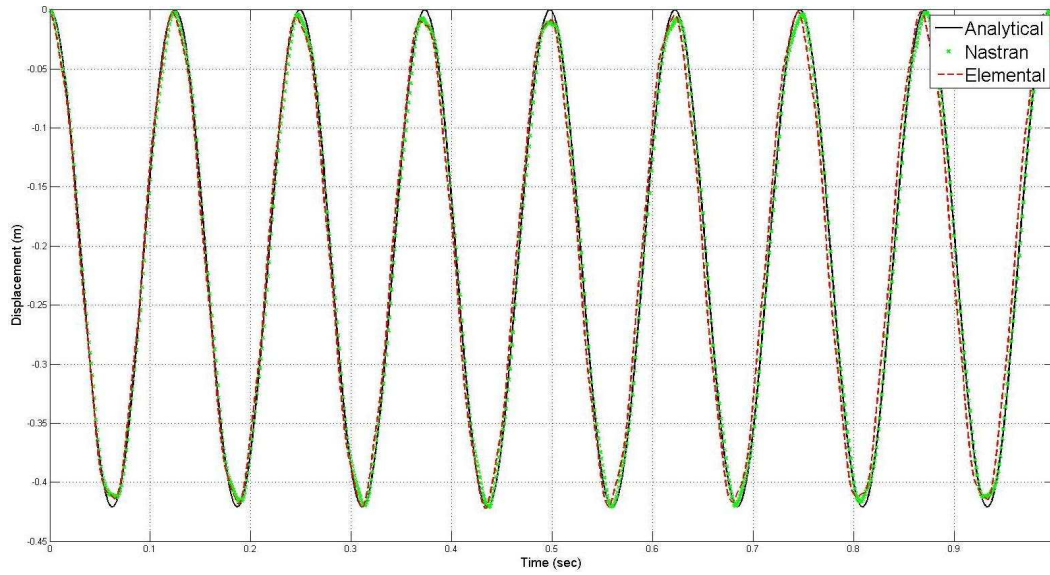


Figure 4.4: Cantilever dynamic response compared to analytical and *MSC Nastran*

4.4 Eigen-Analysis

A clamped in cantilever beam was again considered. This is as an analytical solution for the eigen-values are available (Eq. (4.4)). Using a 10 element mesh, predicted eigen-values are compared to the latter in Table 4.1, proving accuracy of to within 98%.

Table 4.1: Cantilever Modal Analysis

Mode	Natural Frequency (rad/s)		Error %
	Analytical	Elemental	
1	144.78	144.05	0.50
2	903.15	900.26	0.32
3	2528.99	2510.14	0.75
4	4955.50	4890.75	1.31

The modes (Fig. 4.5) were qualitatively assessed against cited cantilever mode shapes (Fig. 4.6) and demonstrated a good correlation. These illustrate the response of the structure when it is excited by its natural frequencies.

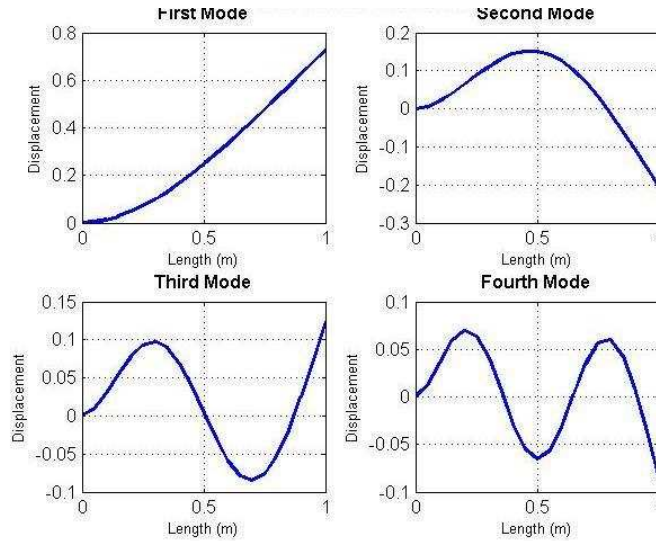


Figure 4.5: Computed mode shapes of Timoshenko cantilever beam

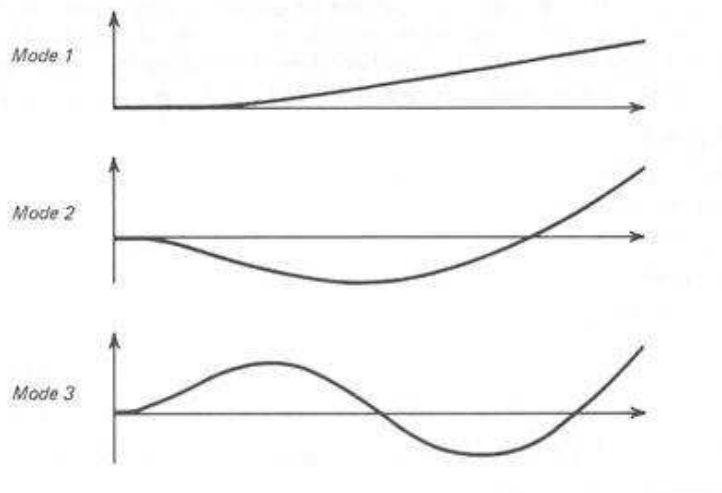


Figure 4.6: Cited [43] mode shapes of Timoshenko cantilever beam

As mentioned in Chapter 3, modal analysis permits a transformation to the frequency domain. Consequently, a dynamic analysis in the frequency domain is compared against the time domain (Fig. 4.7) for the same 2D dynamic beam test case. Mainly, significant computational time savings were achieved, as indicated in Table 4.2, whilst maintaining a high degree of accuracy.

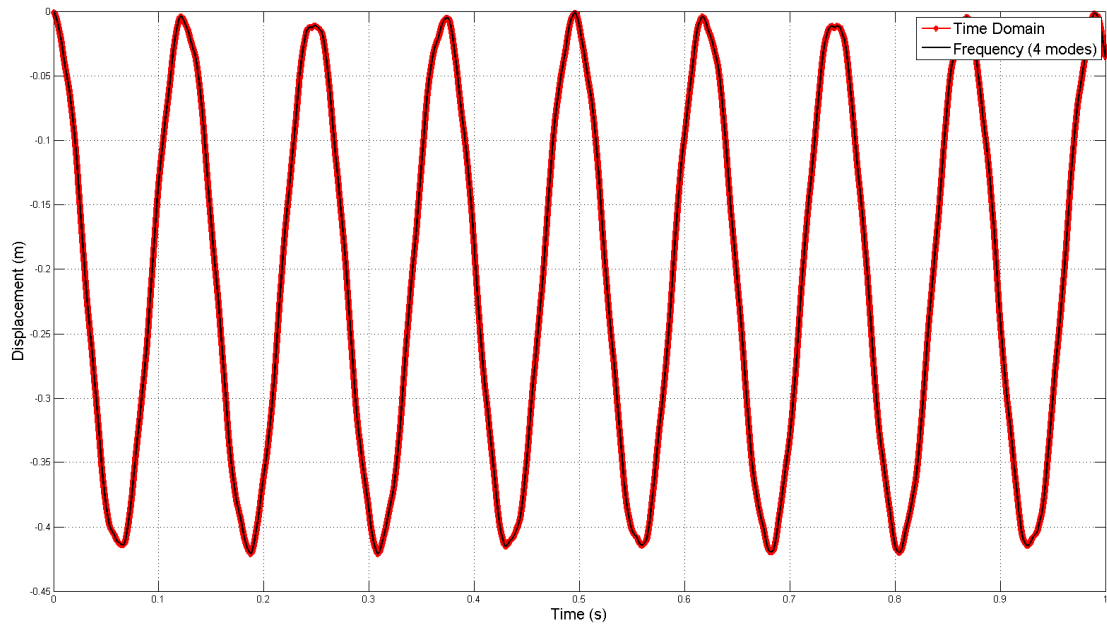


Figure 4.7: Dynamic response of the cantilever free end in time (red) and frequency domain (black)

Table 4.2: Modal Dynamic Analysis Cost Savings

	10 Elements			
no. of time steps	1000	2000	10000	20000
CPU time saved (%)	72.42	74.82	87.47	91.75

The modal analysis software developed is found to be effective and accurate. Both the eigen-values and eigen-vectors provide correct results that aid in the determination of the beam response under various loads. **INSERT time for 100 per cent run and state that times were short and test case employed purely for analysis.**

4.5 Airbus Structure

For the purpose of loads calculations, Airbus employs a condensed aircraft loads model in the form of a beam-stick model (Fig. 4.8). The structural stiffness properties are derived from a high-fidelity FEM mesh of the aircraft which, after static condensation, results in a reduced-order model. It also contains lumped masses to account for inertial components.

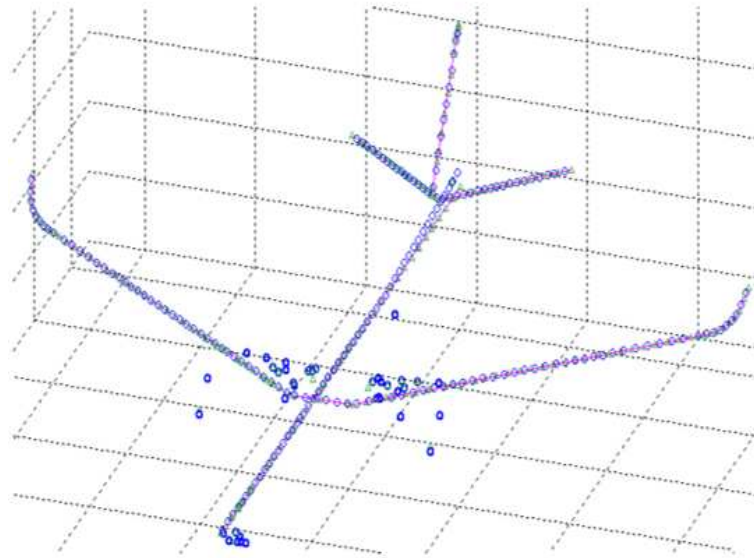


Figure 4.8: Airbus condensed stick model

As previously, a transient analysis was conducted to assess the validity of the numerical software with specific interest in the Airbus structure. However, the response cannot be measured against a numerical solution, thus only a qualitative assessment is completed on an academic test-case. As such, the right wing is isolated (see Fig. 4.9) and subjected to a wing tip load for the first second and subsequently released enabling free vibration to occur. Structural damping is utilised with 2% damping on primary modes as defined in Chapter 3. The initial tip displaces to 0.6m (typical gust displacement) and as shown in Fig. 4.10, the wing tip accelerates quickly to return to its initial neutral position after which damped oscillation occurs. The analysis is assumed to take place in a vacuum resulting in a steep gradient once the tip load ceases. From the results in the figure, the *Elemental*TM code proved stable and robust, while predicting a plausible wing response.

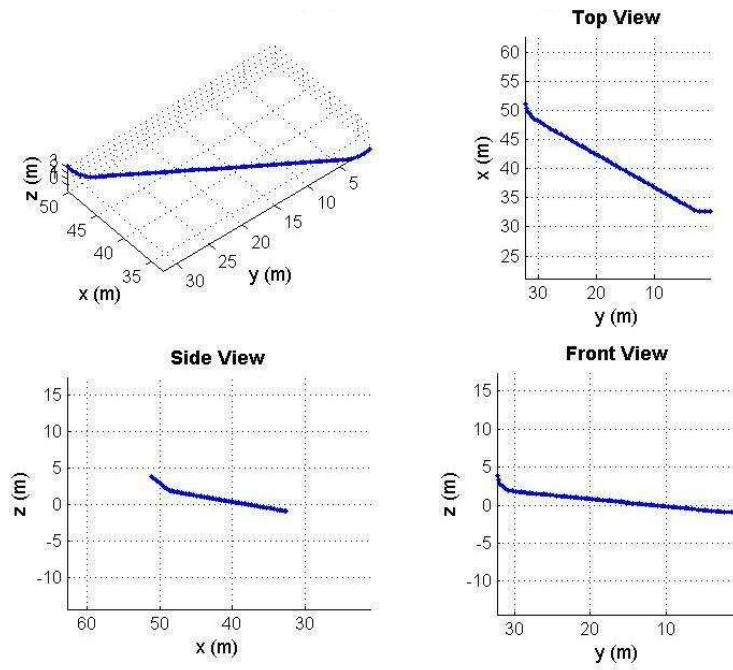


Figure 4.9: Right wing of Airbus structural ROM

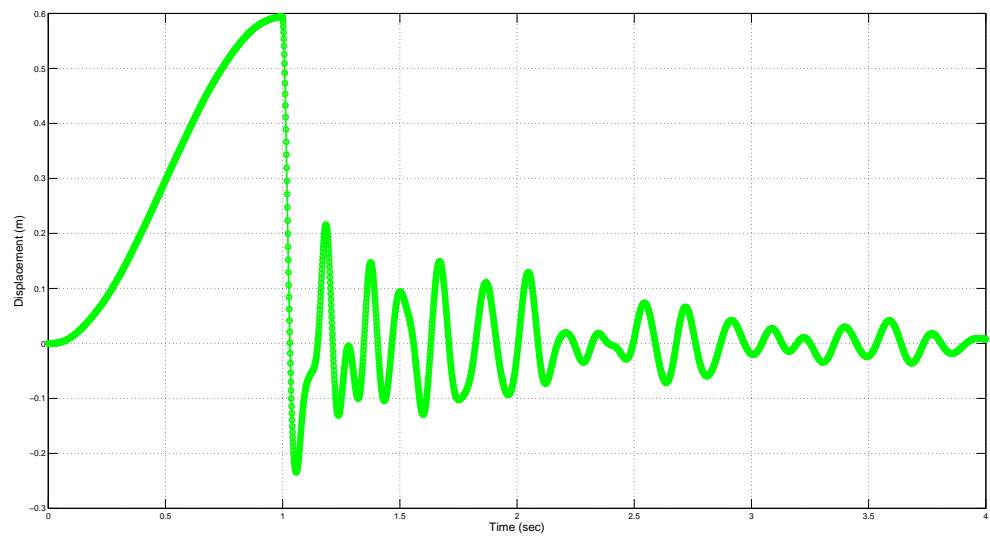


Figure 4.10: Dynamic vertical displacement of right wing tip after being subjected to transient tip load.

4.6 Conclusion

The structural model developed was rigorously evaluated to assess its accuracy. Different test cases, meshes and beam orientations were tested and verified with positive results. It was shown that the developed software accurately determines the static and transient response of a beam under various loads. Modal analysis was also performed on the structure, providing accurate solutions compared to analytical as well as time domain calculations. It is concluded that the structural ROM may be utilised as a platform for fluid-structure interaction and consequent load analysis.

Chapter 5

Fluid-Structure Interaction

5.1 Introduction

The fundamental aim of this project was to commence with the development of a full aircraft model (FAM) for the non-linear loads calculation of an aircraft. In commercial aircraft, fuel can constitute approximately 40% of the take-off weight. Additionally, the sloshing mass of the fuel within wing tanks (Fig. 5.1) may be up to three times larger than that of the wing structure. In order to incorporate the sloshing loads experienced by the structure onto the FAM in an accurate and robust manner, it is essential to employ a strongly-coupled fluid-structure interaction (FSI) scheme. Fluid-structure interaction is the dynamic interaction of a deformable structure with an internal or external surrounding fluid [21]. This involves solving the equations of motion for the solid and the fluid simultaneously [19].

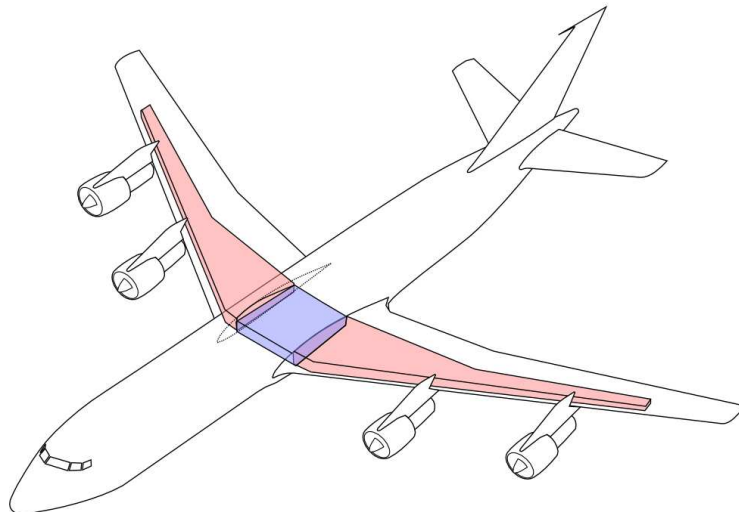


Figure 5.1: Diagram of an aircraft with its center (blue) and wing fuel tanks (red)

Researchers have developed various numerical models in order to represent this interaction [19][21][23], with the two main variants being monolithic and partitioned. The monolithic method involves combining both the structure and fluid sub-domains into one matrix. The fluid and the structure are thus solved concurrently at each time step by means of either a finite volume or finite element discretisation. Resultantly, this enforces strong coupling at the interface. The major disadvantage of this approach is that it may converge slowly due to ill-conditioning [18]. In the author's experience it is also complex both from an algorithmic, as well as implementation point of view.

On the other hand, the partitioned approach utilises separate solvers for the fluid and the structural entities. These solvers then interact with one another at each time step and allow for smaller and better conditioned subsystems to be solved independently [23]. The drawback is that the partitioned scheme does not automatically strictly impose momentum conservation at each sub-iteration leading to potential instability. A major contributor to the instability is the added-mass phenomenon [44]. This corresponds to the mass of the fluid which is accelerated by the structure. Numerous methods have therefore been developed to prevent this instability. Examples of these include Newton-Krylov methods or Gauss-Seidel iterations which provide similar convergence to the monolithic scheme [18]. Notwithstanding the benefit of accuracy and stability that these sub-iteration coupling algorithms achieve, they increase the computational complexity. The latter is due to additional calculations required to compute the Jacobians which correspond to the partial derivatives of flow and structural equations [45].

With regards to this project, the partitioned scheme is the preferred option as it allows for a modular approach. In summary, the structural ROM, which forms the base of the full aircraft model, needs to be linked to the in-house CFD code *Elemental*TM. The structure is discretised via a linear finite-element formulation (Chapter 4) while the CFD solver is discretised by the vertex-centred finite-volume method. Strong coupling at the interface between the two entities will be enforced with a stable algorithm which is relatively simple to integrate into existing Airbus loads calculation processes. The remainder of this chapter is devoted to describing the latter. The chapter is concluded with the development of a fluid-structure model of an actual Airbus wing.

5.2 Fluid Governing Equations

The Navier-Stokes equations dictates the behaviour of the fluid flow. The fluid equations are written in an Eulerian reference frame that are connected to the fuel tanks. In this study, the fluid domain consists of two fuel tanks placed within the wing structure (Fig. 5.1). Therefore, the acceleration experienced by the fuel tank is to correlate to that of the structure. The Eulerian reference frame is to consider the acceleration by incorporating it as a body force. Considering a

viscous, incompressible and isothermal Newtonian fluid, the governing equations are detailed by the continuity (Eq. (5.1)) and Navier-Stokes momentum equation (Eq. (5.2)) as

$$\nabla \cdot \mathbf{u} = 0 \quad (5.1)$$

$$\frac{\partial(\rho\mathbf{u})}{\partial t} + \nabla \cdot (\rho\mathbf{u} \cdot \mathbf{u}) + \nabla p - \nabla \cdot \boldsymbol{\tau} = \rho(\mathbf{g} + \mathbf{a}) \quad (5.2)$$

where ρ , \mathbf{u} , p , $\boldsymbol{\tau}$, \mathbf{g} and \mathbf{a} correspond to the fluid density, fluid velocity, pressure, viscous shear tensor, gravitational and structural (fuel tank) acceleration respectively. These fluid governing equations are discretised by means of an edge-based vertex-centred finite volume method developed in *Elemental*TM. The fluid incompressibility is accounted for by an artificial compressibility algorithm. The exact details and analysis fall beyond the scope of this project, however further reading may be found in [46][47]. For the purpose of this work, the fluid solver may be regarded as a black-box solver that provides an interface pressure after a certain acceleration is applied to it which becomes the acceleration source term i.e. \mathbf{a} .

5.3 Partitioned FSI Interface Treatment

The major source of divergence of a naive partitioned FSI scheme may be described by the following recursive time-advancing process (Fig. 5.2). Firstly, the dynamic fluid flow applies a pressure load onto the solid structure. Due to the applied loads, this structure may deform by an exaggerated amount due to the imposed fluid force not accounting for structural deflection. This may in turn, result in a large negative over-prediction of fluid acceleration. This results in an unstable iterative scheme, which is due to the so-called added-mass effect. Thus, there exists a delay in the fluid force acting on the structure.

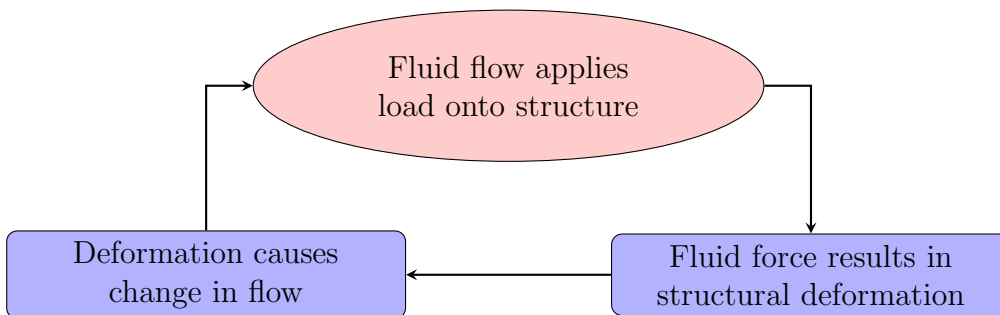


Figure 5.2: Loosely-coupled partitioned FSI scheme

5.3.1 Added-Mass Effect

When considering a structure that interacts with a fluid, the artificial added-mass may be envisaged as an extra mass acting on the structural degrees-of-freedom at the interface [44]. In aircraft fuel tanks the effect varies in a highly non-linear manner according to the acceleration imposed onto the fluid. For instance, if the fluid starts accelerating from rest in the gravitational direction, the additional mass of the fluid onto the structure may be very small. However, if the wing then experiences an upward acceleration, the fluid mass experienced by the wing may be greater than the actual stationary mass. This is reflected on the structural governing equation as follows

$$\mathbf{M}\ddot{\mathbf{U}}^{n+1} + \mathbf{C}\dot{\mathbf{U}}^{n+1} + \mathbf{K}\mathbf{U}^{n+1} = \mathbf{F}_{aero}^{n+1} + \mathbf{F}_{fluid}^{n+1} \quad (5.3)$$

where \mathbf{M} , \mathbf{C} and \mathbf{K} represent the mass, damping and stiffness matrices respectively. The aerodynamic forces acting on the structure are indicated by \mathbf{F}_{aero}^{n+1} and the fluid slosh force by, \mathbf{F}_{fluid}^{n+1} . In the case FAM computations, the above would result in an unstable solution if solved in a sequentially staggered partitioned manner as previously stated. Ironically, decreasing the time step size causes an increase in the instability due to an increase in the added mass operator applied to the implicit structural solver [48]. The instability grows exponentially implying that the smaller the time step size, the quicker violent instability will be apparent. Including approximations of the force within each time step has been suggested and may be found accurate for some partitioned problems [49]. Various predictor-corrector algorithms have also been utilised to minimise the onset of the unstable nature of the FSI model by predicting structural displacements [21]. Stability may also be asserted by employing Newton-Raphson iterations between solvers. Although these coupling algorithms may provide a stable solution, they are typically complex to implement for the application considered here.

5.3.2 Proposed Algorithm

In order to alleviate the instability of a partitioned scheme and ensure strong coupling at the interface, a simple robust coupling scheme is proposed. It hinges on inserting an added-mass onto the structure that mimics the effect of the fluid. Additionally, a simple algorithm is sought that requires minimal changes to the complex CFD slosh solver. Therefore, instead of utilising forces to be transferred between entities, an added inertial fluid mass, which is included in the structural equations, is computed as

$$m_f^{\tau+1} = \frac{\partial m}{\partial a} (a^{\tau+1} - a^\tau) + m_f^\tau \quad (5.4)$$

where m_f represents the artificial fluid mass obtained from the CFD solver and τ represents the iteration counter within a time step that allows for the mass to

converge. Note that the process commences with an initial guess for m_f^τ which comes from the CFD solver (as detailed below). Since the solution is driven to pseudo-steady state, $m_f^{\tau+1} = m_f^\tau = m_f^{n+1}$ upon convergence and may be included as the fluid mass on the left-hand side of the structural governing equations (Eq. (5.3)). The term $\frac{\partial m}{\partial a}$ refers to the numerical approximation of the inertial mass and sensitivity to acceleration and is easily computed as

$$\frac{\partial m}{\partial a} = \frac{(m^{\tau+1} - m^\tau)}{(a^{\tau+1} - a^\tau)} \quad (5.5)$$

The interaction between the two entities are strongly-coupled at each time step due to the artificial added-mass converging between time steps. The CFD solver is to return the added masses. To this effect, an array of artificial added masses are created as depicted in Fig. 5.3. The mass, m_f , is computed from the fuel related pressures on the tank wall in the zone around each mass. The following equation is employed for this

$$m_f = \mathbf{F}_{fluid}^{\parallel} / a \quad (5.6)$$

where $\mathbf{F}_{fluid}^{\parallel}$ is the zonal fluid slosh force in the direction of the tank acceleration in that zone. The added masses are subsequently passed to the structural solver as point masses. These only compensate for the force in the direction parallel to the acceleration. The total fluid force (\mathbf{F}_{fluid}^{n+1}) comprises of the parallel ($\mathbf{F}_{fluid}^{\parallel}$) and perpendicular ($\mathbf{F}_{fluid}^{\perp}$) components. Forces perpendicular to the acceleration are computed as previously discussed. The added fluid mass from Eq. (5.4) and perpendicular force will then be substituted into Eq. (5.3) as

$$(\mathbf{M} + m_f^{n+1}) \ddot{\mathbf{U}}^{n+1} + \mathbf{C}\dot{\mathbf{U}}^{n+1} + \mathbf{K}\mathbf{U}^{n+1} = \mathbf{F}_{aero}^{n+1} + \mathbf{F}_{fluid}^{\perp} \quad (5.7)$$

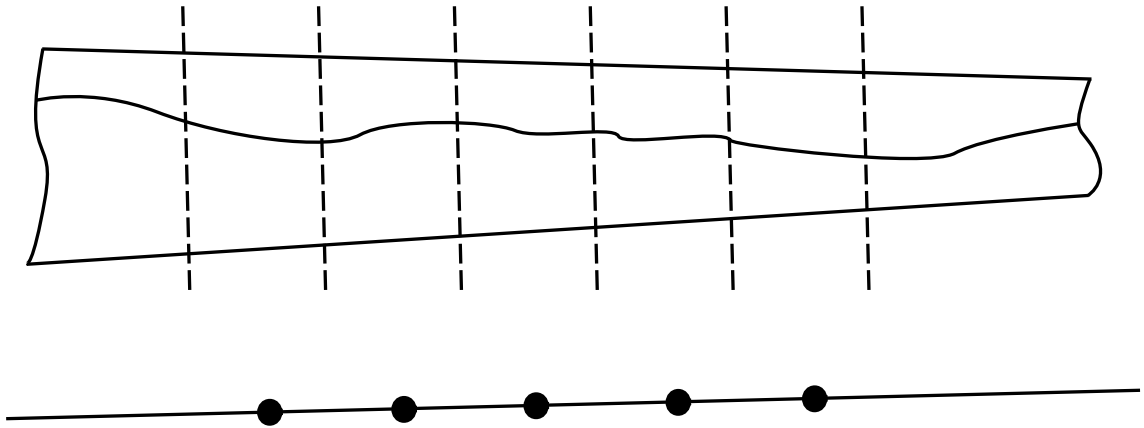


Figure 5.3: Sloshing tank section with zones (top) corresponding to an associated added mass on the structural ROM (bottom)

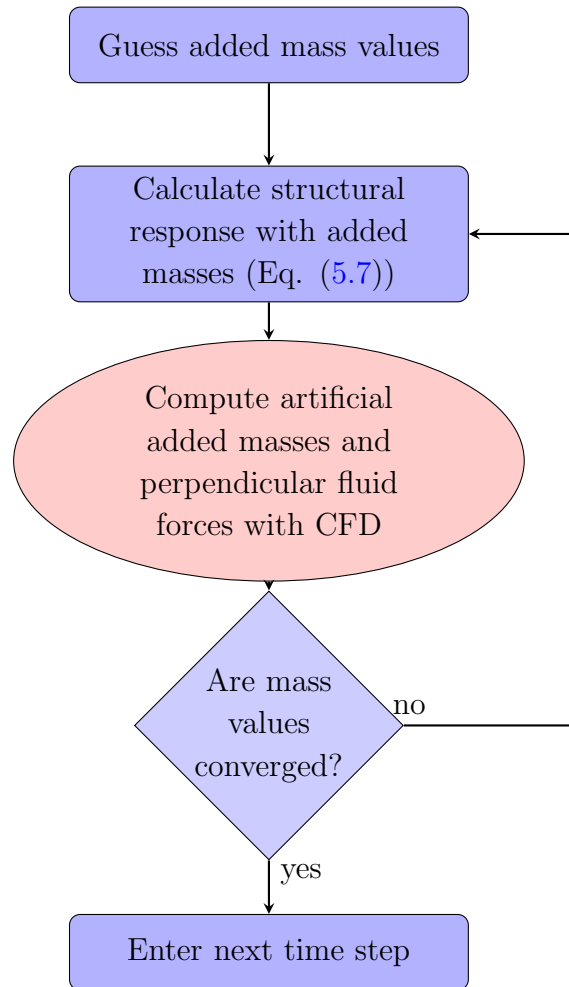


Figure 5.4: Proposed strongly-coupled partitioned FSI scheme

5.4 Industrial Application

The above model is now applied to an actual Airbus wing. The wing structure is a three-dimensional ROM representation of an Airbus aircraft wing shown in Fig. 5.5. It is assumed clamped in at the root, and constructed by incorporating the coordinate locations, mass and stiffness values obtained from Airbus MSC Nastran data files. The wing consists of two separate tanks, namely the centre tank and the wing tank, also known as a feed tank. For the purposes of this work, these are approximated via two 2D tanks (Fig. 5.6) that run along the centre line (dotted line in Fig. 5.5) of the wing. The width of the tank (3rd dimension not) is taken as the average chord length of each tank. The two tanks are shown superimposed onto the structural ROM in Fig. 5.7. For the purposes of this work, the aerodynamic loads are also neglected and replaced by prescribing a vertical displacement at the wing root. This data is provided by Airbus from in-house FAM gust response calculations.

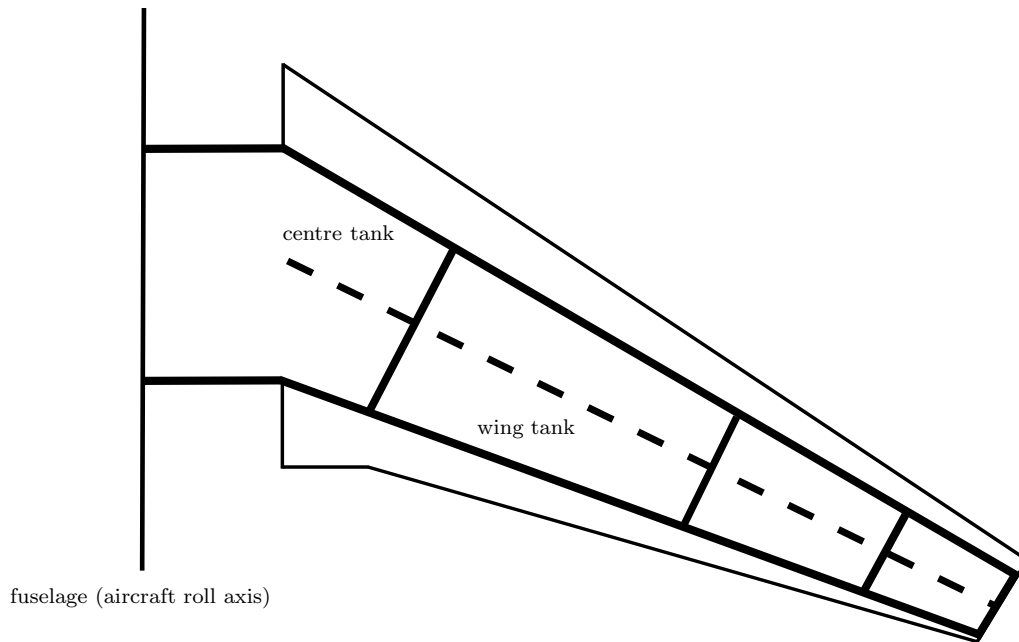


Figure 5.5: Top view representation of an Airbus aircraft wing and wing tanks



Figure 5.6: Front view representation of an Airbus aircraft wing tanks

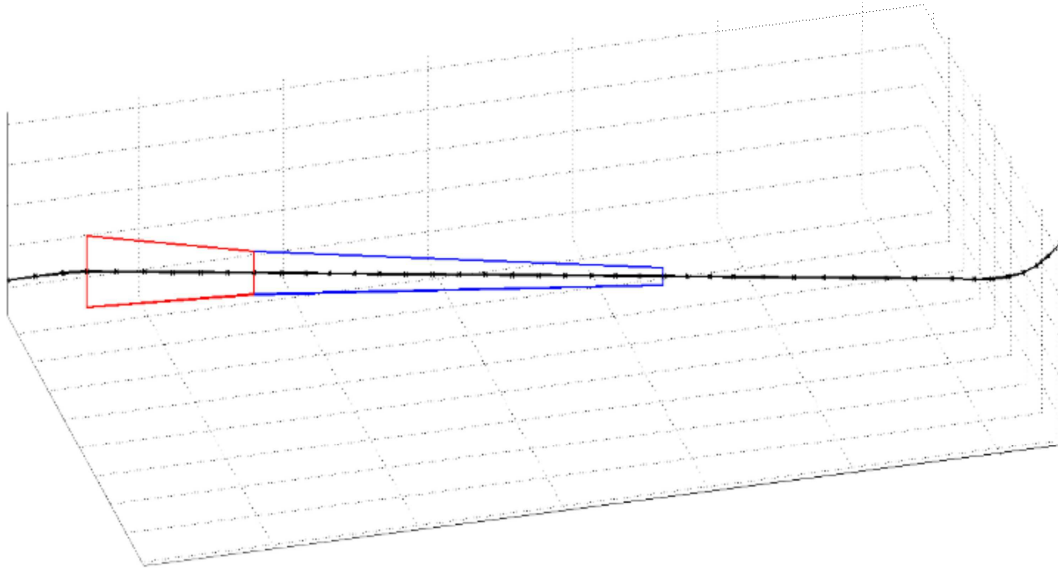


Figure 5.7: Diagram of an Airbus aircraft wing coupled to its center (red) and wing fuel tanks (blue)

To model the real-life interaction between the two subsystems, approximate accelerations (computed from the structural ROM) are transferred to the tanks while tank forces are returned in the form of added masses. With regards to the former, only planar accelerations (Fig. 5.8) are applied to the central tank. This is appropriate to the gust condition to be simulated in this work (which is purely vertical in nature at the wing root). The wing tank, on the other hand, experiences rotation due to wing flex, and is therefore provided with both rotational and translational components (Fig. 5.9). These are approximated via linear interpolation of the accelerations of the structure at the wing tank inboard and outboard locations. In addition to the above accelerations, a constant gravitation acceleration is to be applied, which is a function of wing incline. This is applied to both tanks, as per Fig. 5.10, and changes during the simulation due to wing flex.

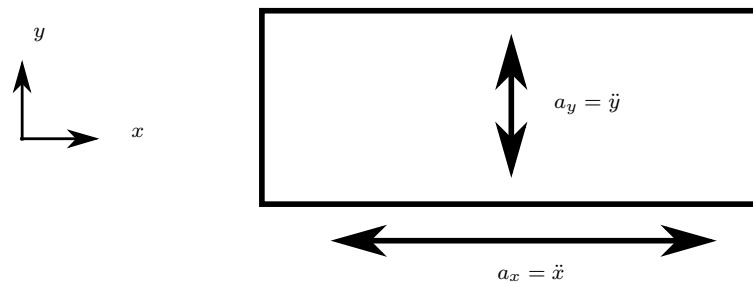


Figure 5.8: Translational acceleration of the centre fuel tank

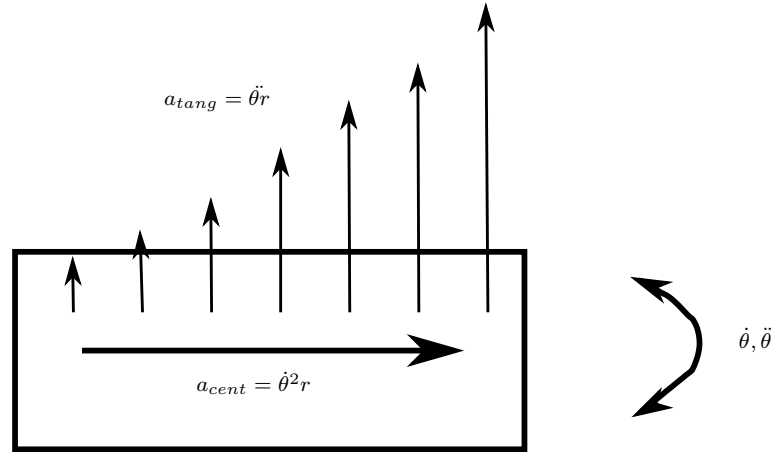


Figure 5.9: Rotational acceleration of the wing fuel tank

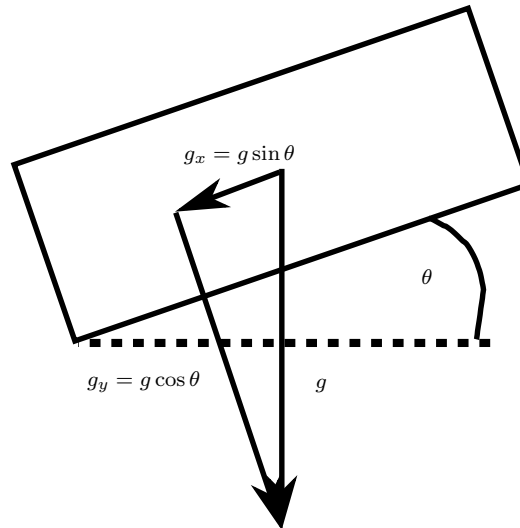


Figure 5.10: Gravitational acceleration components of the fuel tank

From the above, the following accelerations are therefore applied to the CFD solver

$$a_x = \ddot{x} + a_{cent} - g_x = \ddot{x} + \dot{\theta}^2 r - g \sin \theta \quad (5.8)$$

$$a_y = \ddot{y} + a_{tang} - g_y = \ddot{y} + \ddot{\theta} r - g \cos \theta \quad (5.9)$$

where a_x and a_y represent the acceleration that the fuel tank experiences in the horizontal and vertical direction respectively. The subscripts, *cent* and *tang* denote the centrifugal and tangential acceleration of the tank due to its rotation. Lastly, the gravitational acceleration is denoted by g .

5.5 FSI Solution Procedure

The solution procedure for the strongly-coupled partitioned FSI system requires solving of the fluid and solid governing equations in a time-stepping manner. Additionally, an approximation of the mass of the fluid is completed at each time step that effects strong coupling. The entire process is detailed as follows:

1. The solid discrete equation (Eq. (5.7)) is solved under the influence of a gust load (applied here as a vertical acceleration at the wing root). The artificial added masses are included subject to gravitational acceleration only using an initial guesstimate (typically the mass of the fuel). This results in the solution for the displacement, velocity and acceleration at the interface.
2. The fluid governing equations (Eqs. (5.1) and (5.2)) are solved for an iteration via the CFD code. This provides the artificial added masses and perpendicular forces due to the wing acceleration.
3. The solid equation is solved again with the inclusion of the newly CFD-computed added masses and extra force components. The added masses are computed by employing Eq. (5.6) as well as incorporating the inertial mass effects (Eq. (5.5)).
4. Steps 2 and 3 are repeated for each time step until the computed wing displacement no longer changes between iterations.

5.6 Conclusion

In this chapter a strongly-coupled partitioned fluid-structure interaction scheme was developed. A pragmatic algorithm was implemented to overcome the problematic added-mass phenomenon in strongly-coupled partitioned problems. The governing equations for the fluid and the structure were discretised with a FVM and FEM approach respectively and were linked within *Elemental*TM via the coupling scheme proposed.

Chapter 6

Fluid-Structure Interaction: Results and Evaluation

6.1 Introduction

In this chapter, the validation and verification of the proposed strongly-coupled algorithm is documented. Initially, the one-dimensional dynamic piston-channel problem [50] is utilised as a benchmark test-case for strongly-coupled fluid-structure interaction (FSI). The predicted results of the partitioned method were compared to the analytical solution that exists for this case. Next, an industrial problem is modelled which involves the Airbus wing (described in the preceding chapter) subject to a large vertical gust load.

6.2 Piston-Channel Problem

The dynamic piston-channel problem provides numerous difficulties when attempting to model it in a partitioned manner due to the strong interaction between the fluid and the solid. This test-case assumes an elastic piston, of length $1m$, that transposes an incompressible fluid out of a frictionless channel, of length $10m$, at the free end (see Fig. 6.1). The solid is prescribed a velocity at its left end of $v(t) = 0.2t \text{ m.s}^{-1}$, which results in a constant acceleration. The solid has a Youngs Modulus of $E = 10Pa$ while the density and Poisson's ratio is assumed negligible i.e. $\rho_s = 0$ and $\nu = 0$. The fluid component has a density of $\rho_f = 1kg.m^{-3}$.

This problem may be simplified to a 1D spring-mass system, as seen in Fig. 6.2, with an elastic spring and a time-dependent mass which permits an analytical solution to be sought. The system may be described by the following equation of motion

$$k(u_{int} - u(t)) = -m \frac{dv_{int}}{dt} \quad (6.1)$$

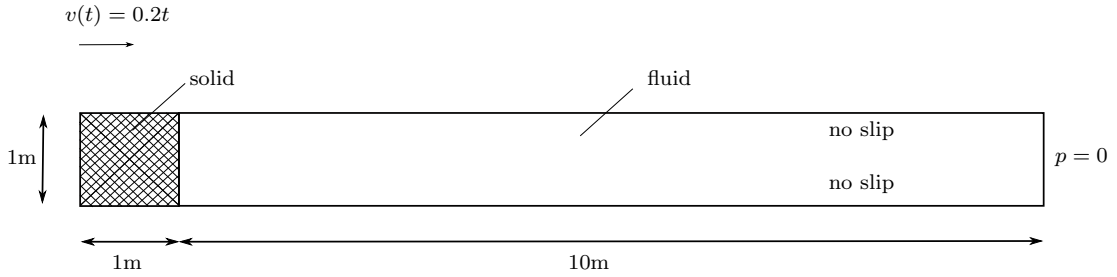


Figure 6.1: Piston-Channel problem with boundary conditions

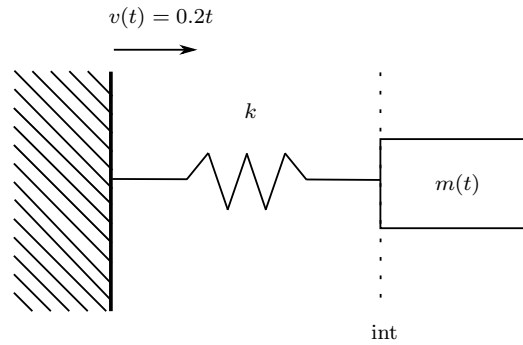


Figure 6.2: Mathematical representation of the piston-channel problem

where the displacement and velocity of the interface are represented by u_{int} and v_{int} respectively, while k corresponds to the equivalent stiffness value, m to the mass of the fluid. Lastly, the prescribed displacement of the left wall is $u(t)$. The simplified equation (Eq. (6.1)) may be represented by the coupled first-order differential equations (Eqs. (6.2) and (6.3)) and can be solved via the Runge-Kutta method.

$$\frac{dv_{int}}{dt} = \frac{10(u_{int} - 0.1t^2)}{(u_{int} - 10)} \quad (6.2)$$

$$\frac{du_{int}}{dt} = v_{int} \quad (6.3)$$

The analytical results from the simplified spring-mass system are compared to the numerical results of the proposed strongly-coupled partitioned scheme. With regards to the latter, the solid was modelled as a simple spring structure via the Newmark method and the fluid by a time-dependent mass, which is essentially a function of acceleration. For the first iteration of the first time step this was taken as 10% of the actual mass (a smaller value could also be employed and yielded similar results). The results indicate accurate correspondence to the analytical solutions, as depicted in Fig. 6.3. The stability of the numerical scheme is also a critical component that needs to be assessed. For this purpose, various time steps were employed and all demonstrated a stable solution (Fig. 6.4), albeit

inaccurate for larger time steps. The stability and robustness of the scheme are further revealed by the number of iterations required to allow the mass residuals to converge within a time step (Fig. 6.5).

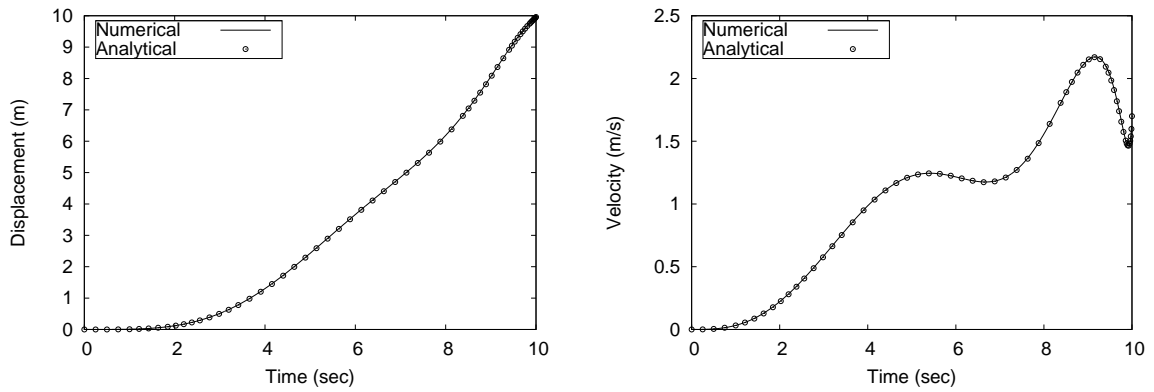


Figure 6.3: Displacement (left) and velocity (right) of the interface of the piston and channel

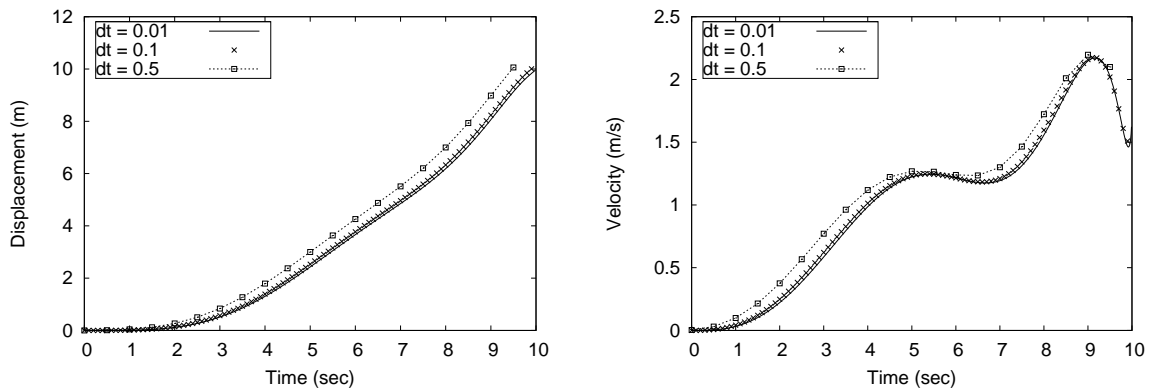


Figure 6.4: Displacement (left) and velocity (right) of the interface of the piston and channel with various time step sizes

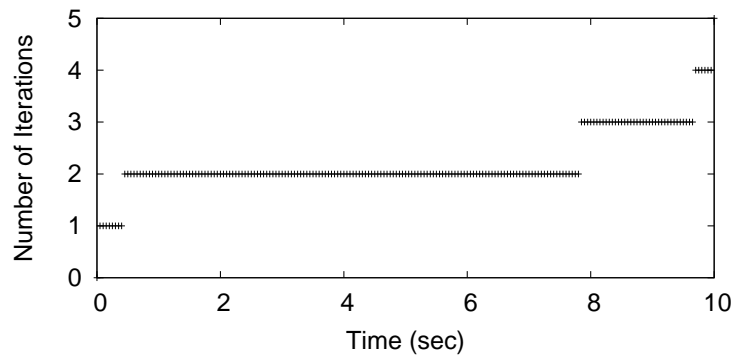


Figure 6.5: Number of iterations required per time step for the mass residuals to converge

6.3 Industrial Application

The FAM developed in this work represents a loads analysis platform incorporating fully non-linear slosh forces. As an initial implementation, this platform aims to demonstrate the computational software to be robust and stable, while indicating differences in computed response as compared to the "full tank" approach. For the purpose of this project, the wing structure is coupled to its interior fuel tanks filled to 75% and 25% and exposed to an aerodynamic gust condition, as displayed in Fig. 6.6. As noted previously, the latter is simulated via prescribing vertical accelerations to the wing root (which is clamped in). This data is as provided by Airbus. The computed response is subsequently compared to the full tank approach often employed.

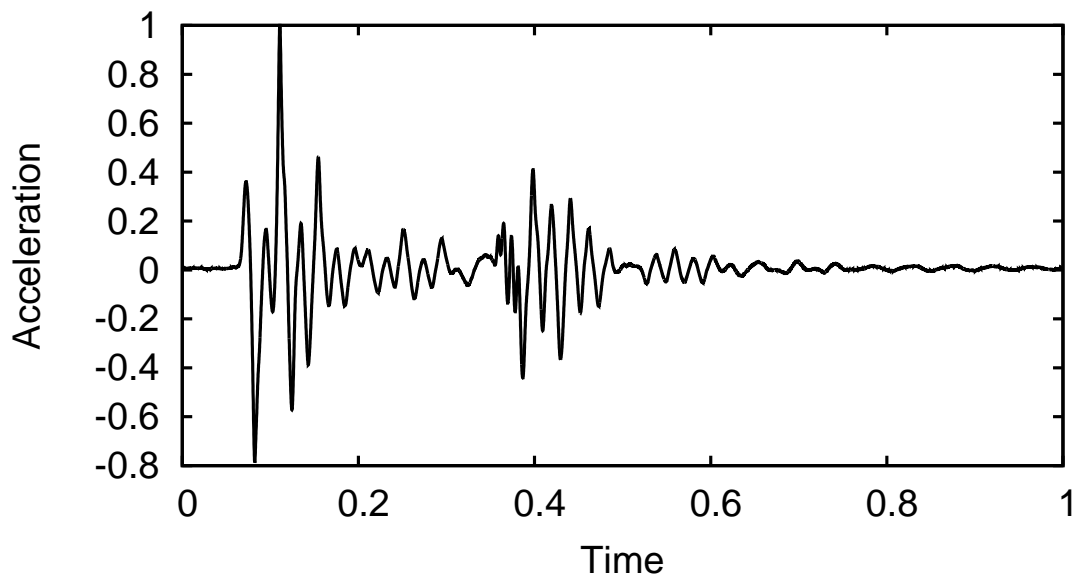


Figure 6.6: Real-life gust profile imposed as wing root acceleration (axes in terms of normalised acceleration and time)

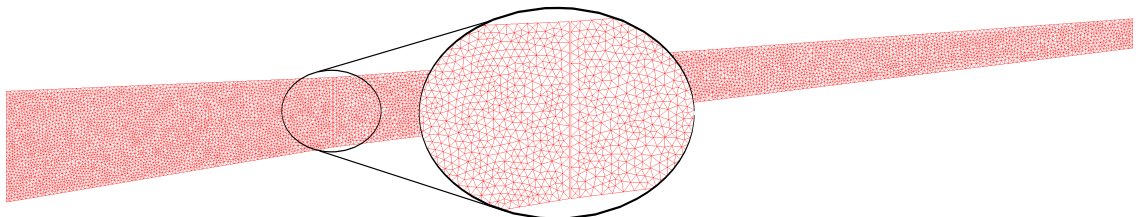


Figure 6.7: Unstructured mesh for vertical sloshing (13,430 nodes)

The wing was represented using a time-domain FEM model, and masses and stiffnesses read in from Airbus MSC Nastran data files, as stated previously. The frequency domain was not applied due to difficulties in computing the higher modes of the wing. Further research is required here and recommended for future work. Prior to the computational modelling via *Elemental*TM, the continuous space describing the fuel tanks is broken up into an assemblage of connected nodes forming elements. This constitutes a mesh that aims to capture the fluid flow properties accurately. For this purpose, a fine, unstructured mesh consisting of 13,430 nodes was created as illustrated in Fig. 6.7. This mesh was selected subsequent to a short mesh independent study, but should be assessed for further refinement as part of future work. As mentioned, the tanks were filled to 75% (Fig. 6.8) and 25% (Fig. 6.9).

It may be noted that the baffles, present in standard aircraft wing tanks, are neglected in this project to limit the scope of work. Vents are accounted for by prescribing atmospheric pressure to the top right node of each tank. The kerosene jet fuel and air are contained within the tank. The respective properties at a cruising altitude of 12,000 *m* are displayed in Table 6.1. For the sake of confidentiality, all graphs displayed are normalised. The pressure and displacement graphs are normalised to the maximum overall pressure and maximum vertical displacement (*z*-direction) respectively.

Table 6.1: Table of fluid and gas properties at 12,000 *m* above sea-level

Property	Density ρ (kg/m^3)	Viscosity ν ($Pa.s$)
Fuel	810	$6.48 e^{-4}$
Air	0.3042	$1.44 e^{-5}$

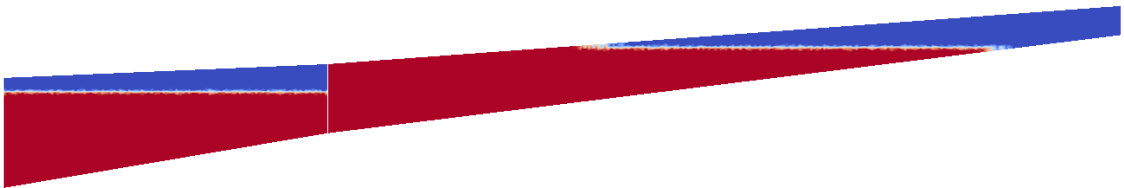


Figure 6.8: Aircraft wing tanks with 75% fill level

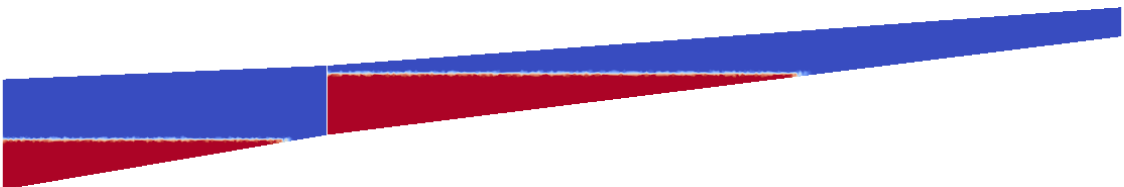


Figure 6.9: Aircraft wing tanks with 25% fill level

The computed wing displacement response at the wing tip is compared to the typical full tank model in Figs. 6.10a, 6.10b and 6.10c. It is noted that the 100% filled tank produces a greater wing tip displacement in all three directions, by up to 30%, compared to the wing coupled to the partially filled tanks. The dynamic response of the wing tip in the vertical direction (z -direction) corresponds to the applied gust load trajectory and consequently the maximum wing tip displacement occurs in the same direction. In the vertical orientation, both the 75% and 25% cases produce relatively similar responses to one another with very slight differences in frequency and amplitude ($< 5\%$), which was surprising. This is ascribed to the sloshing fuel within the partially-filled tanks remaining very close to the fuselage location for both fill levels (Figs. 6.8 and 6.9). Conversely, the full tank has more mass distributed further along the wing to the wingtip, resulting in a greater displacement.

Although the gust acceleration is purely vertical, displacement of the wing along the fuselage (x -direction) and in the horizontal direction (y -direction) arise due to the wing's swept back orientation in three dimensions. Moreover, the offset winglet induces a torsional wing response that increases the deflection in all three directions. The increased deflection of the wing with full fuel tank can be attributed to the mass of the fuel adding inertia to the structure. The additional mass also decreases the natural frequency of vibration of the structure. This results in an increased period of vibration (Fig. 6.10a) due to the inversely proportional relationship between period and frequency. Additionally, when violent sloshing regimes are induced, the fluid may impact the tank and exacerbate or diminish the wing displacement, depending on the type of acceleration experienced. The acceleration imposed on the fuel tanks prompts fuel slamming during the period of high acceleration. This is evident in Fig. 6.10a, where during normalised time of 0.2-0.5, the 75% case experiences a reduced structural vibration compared to the 25%. This period of reduced wing tip displacement corresponds to duration of the input gust where the highest acceleration is imposed onto the wing structure. In contrast however, after 0.5 units of normalised simulation time, the deflection of the 75% fill level case is exacerbated by the impact slosh.

This specific applied gust load elicits a wing tip displacement within the small angle regime as the angle produced at maximum displacement is less than 5° . This is due to the wing stiffness decreasing from very stiff at the fuselage to more flexible at the wing tip. The full tank produces a smooth and linear wing response, while the sloshing tanks induce non-linearities in the computed wing tip displacement, as shown in Figs. 6.10b and 6.10c. These non-linearities is attributed to the sloshing fuel contained within the wing tank. Even though the wing displacement remains within the small angle limit, higher modes may be excited in the wing structure due to the coupled slosh analysis computed by the CFD solver. As such, it is recommended to extend the beam theory utilised to encompass non-linear deformation.

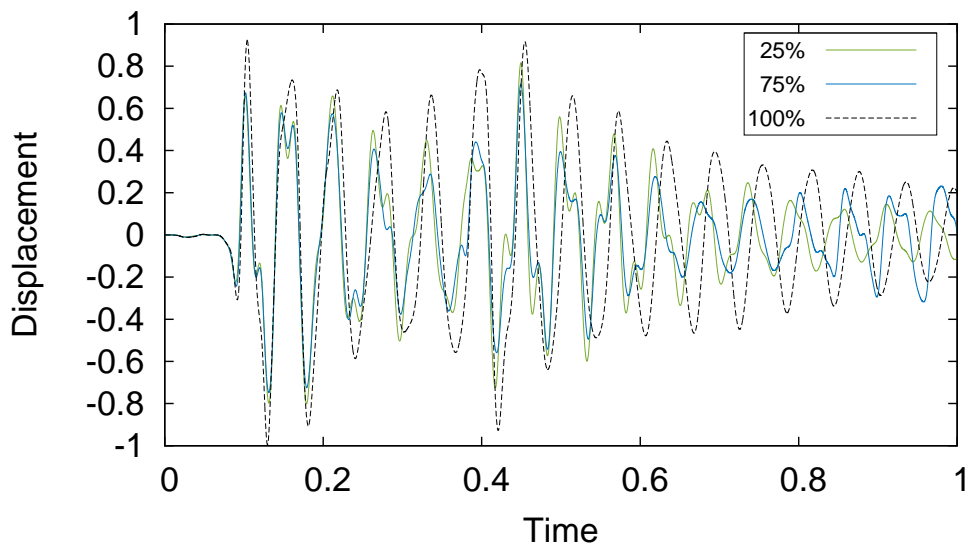
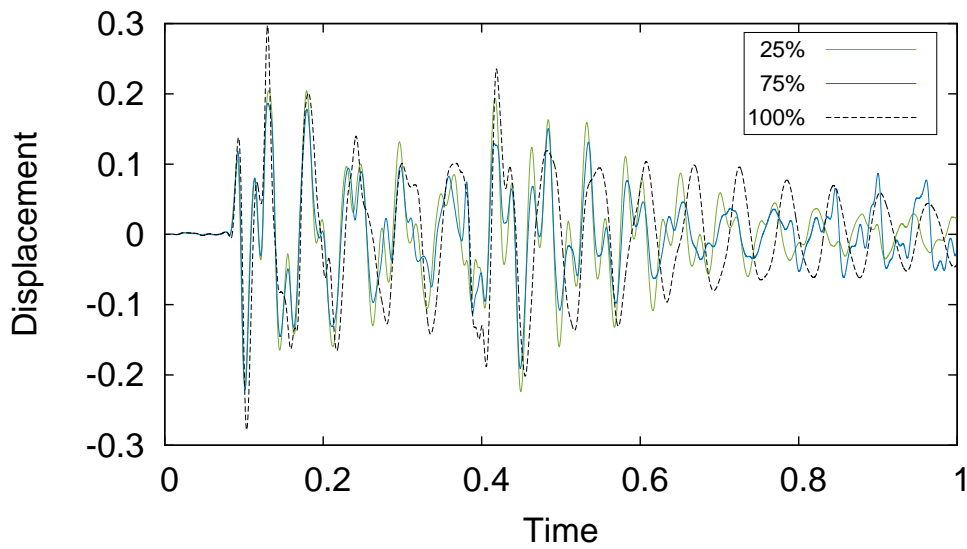
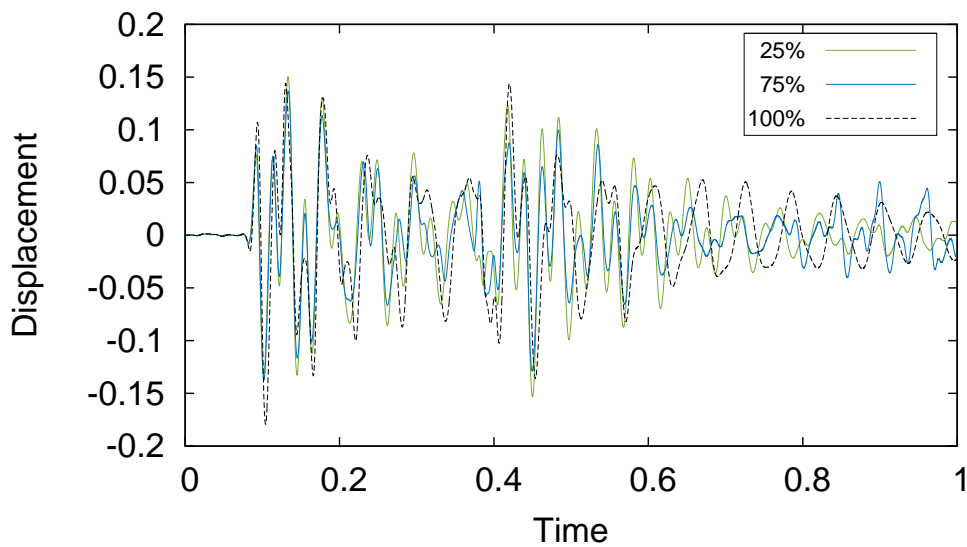
(a) Vertical (z -direction) wing tip deflection(b) Horizontal (y -direction) wing tip deflection(c) Wing tip deflection in the direction along the fuselage (x -direction)

Figure 6.10: Wing tip deflection in vertical (top), horizontal (middle) and along the fuselage (bottom) direction for various tank fill levels

A comparison between the input gust and average vertical acceleration of each tank is shown in Figs. 6.11 and 6.12. These exhibit sporadic and non-linear behaviour in comparison with the smoother input gust. Due to the sloshing impact and heavier fluid mass, the 75% test case produces larger and more erratic tank accelerations compared to the lower fill level case. Tank accelerations also generate dynamic fluid pressures on the tank walls. The variation in pressure of each tank was assessed by determining the fluid pressure at the base of each tank, indicated by the pressure probe locations in Fig. 6.13. The blue and red denote the center and wing tank base locations respectively. The calculated normalised pressures are depicted in Fig. 6.14. Firstly, the fluid pressure is representative of the applied gust acceleration, thus satisfying the initial test of validity. Secondly, the pressure loads align with the general assumption that the 75% fill level test-case produces greater pressures compared to the 25% case.

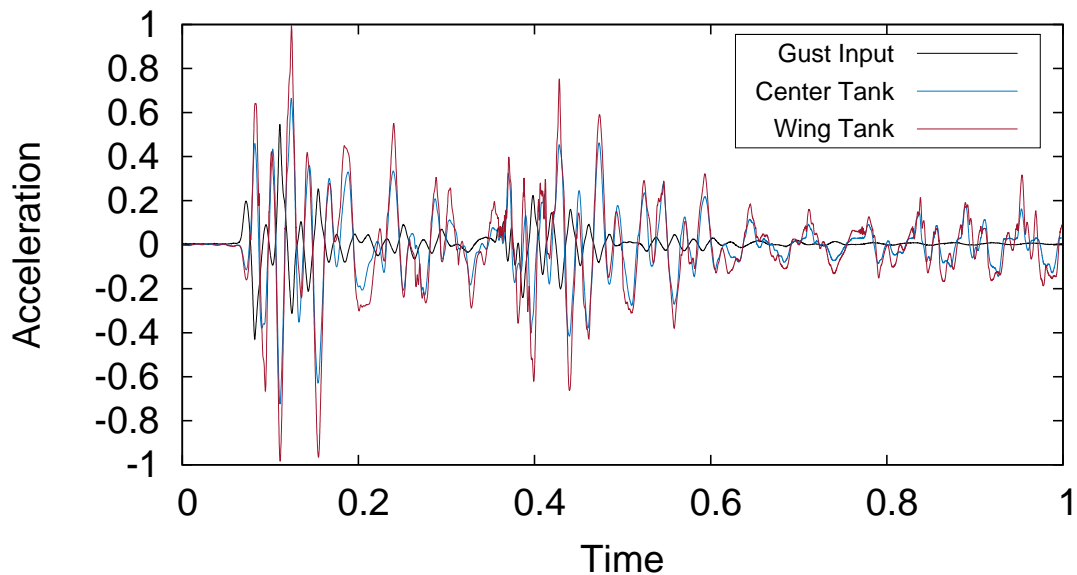


Figure 6.11: Input gust compared to center and wing tank acceleration for 75% filled tank

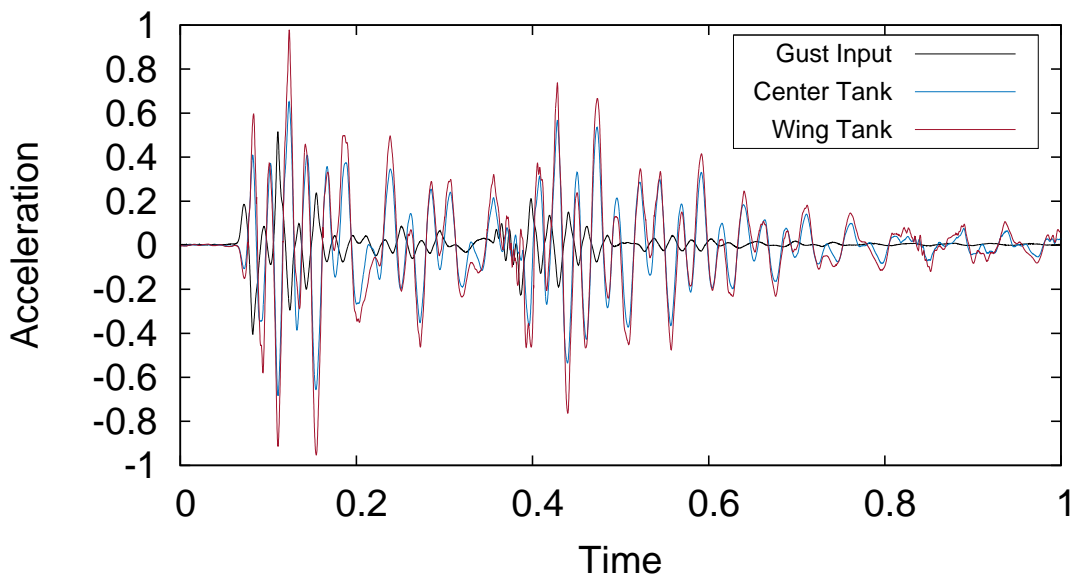


Figure 6.12: Input gust compared to center and wing tank acceleration for 25% filled tank

Moreover, it is observed that for the higher fill-level case, the center tank produces a higher maximum pressure, while for the 25% case, the wing tank has a higher maximum pressure. This is primarily due to the tank geometry which allows for a greater maximum allowable pressure due to the vertical height of the tank at the locations, as depicted in Fig. 6.15. Another contributing factor is the low fluid acceleration in the horizontal direction (y -direction), resulting in minimal horizontal fluid motion in the tank which could increase the pressure.

The major cause of horizontal fluid motion is due to centripetal acceleration of the rotation. For this test-case, the latter proves insufficient to cause significant lateral impact slosh for the 75% fill case, as shown in Fig. 6.15. On the other hand, the 25% case (Fig. 6.15) does not induce violent slosh as the location of the fluid is close to the fuselage which experiences lower accelerations.

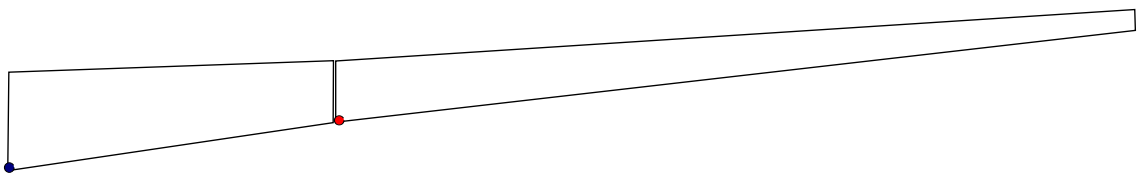


Figure 6.13: Pressure locations of the center (blue) and wing (red) tanks

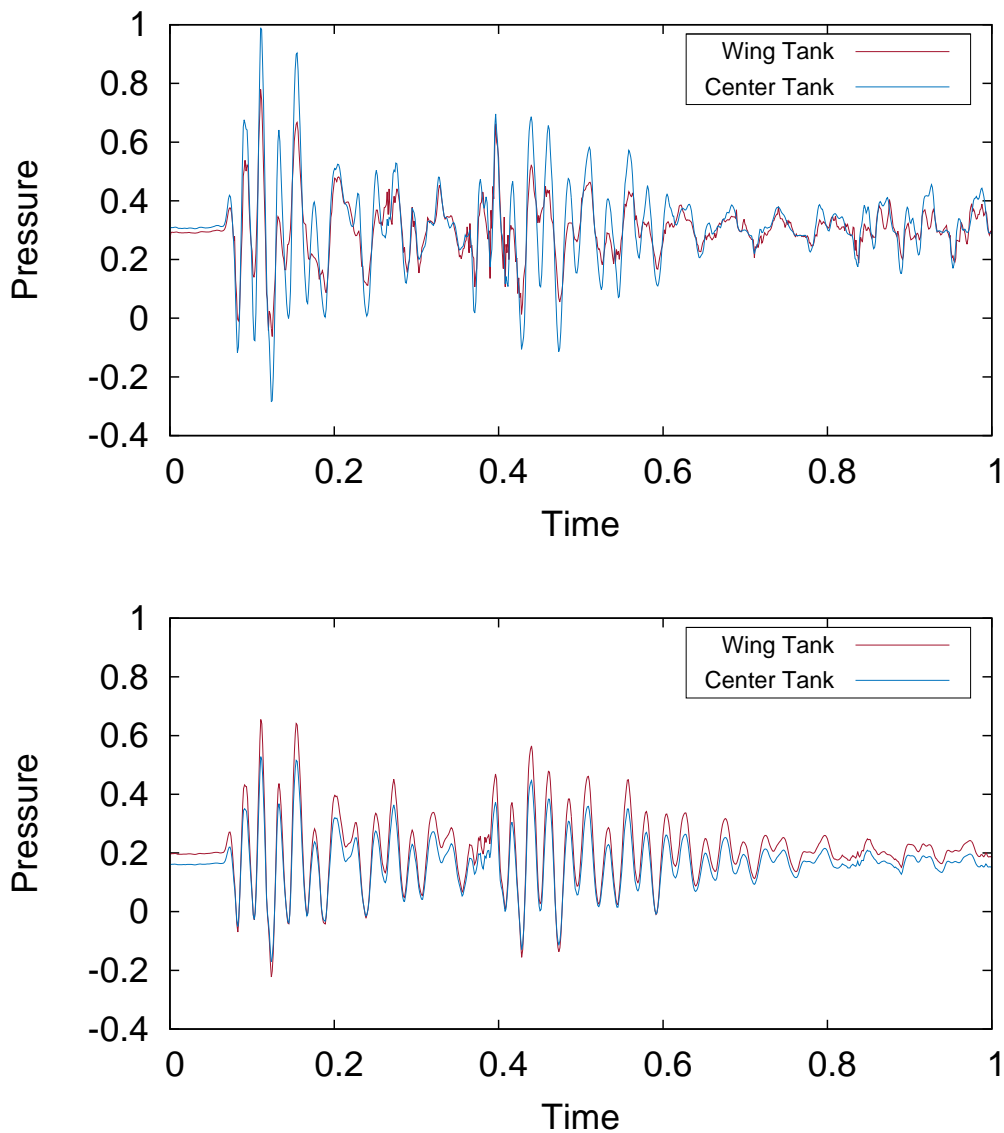


Figure 6.14: Normalised pressure at the identified tank locations for 75% (top) and 25% (bottom) fill level tanks

Although computational time was not critical in this project, a comparison is apt to demonstrate the context of the FAM technology. An increase in computational time of 66% is observed when comparing to the Airbus FAM with full tank (no CFD calculations). All simulations were completed on a desktop notepad with an i7, quad-core, 2.3 GHz *Intel* processor.

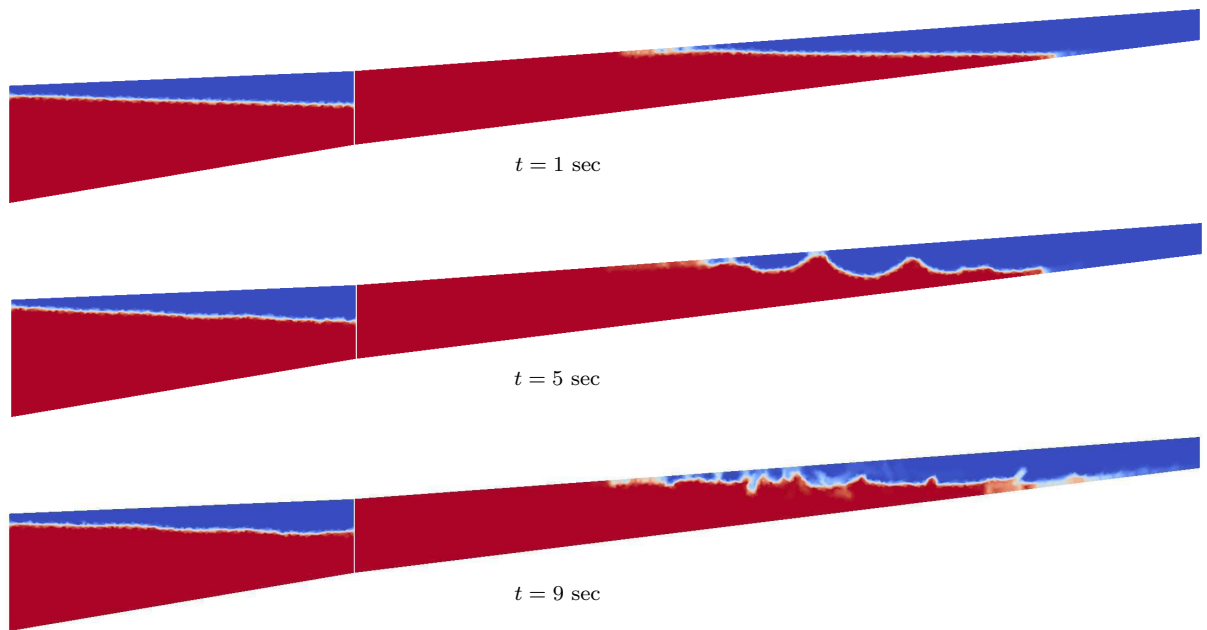


Figure 6.15: Interface representation of 75% filled tank at the various time steps

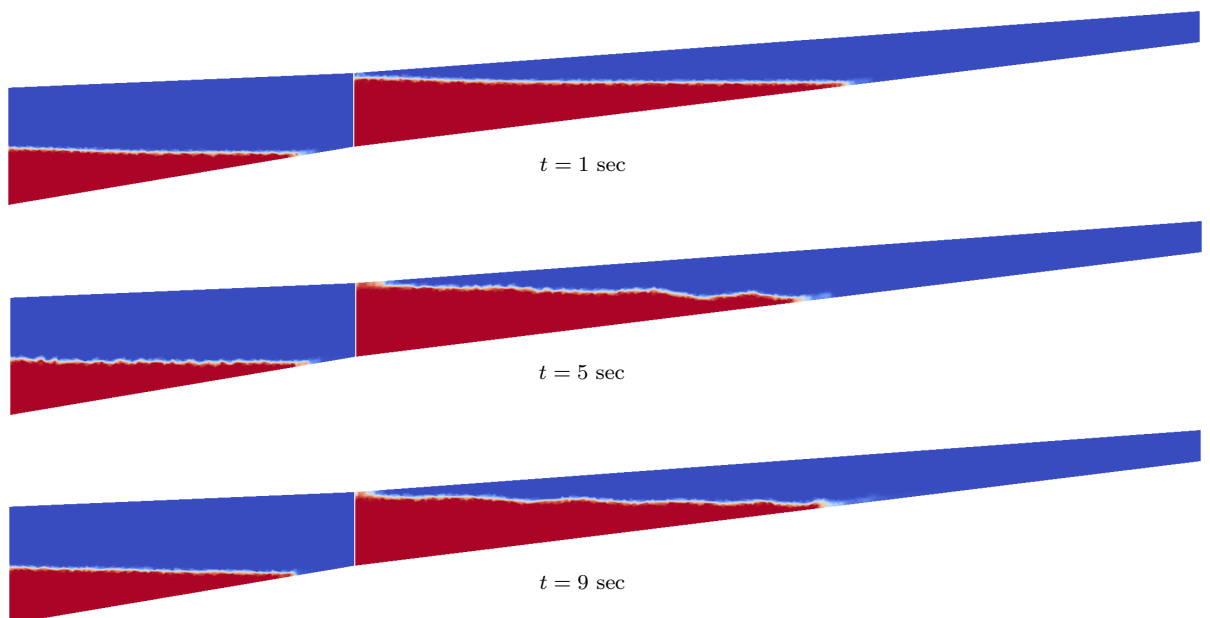


Figure 6.16: Interface representation of 25% filled tank at the various time steps

6.4 Conclusion

In conclusion, the loads analysis platform exhibits robust and stable results. The pressure and interface position was analysed for the fluid component while the structural response was also deemed appropriate. Significant differences were observed if compared to the full-tank model. These included up to 20% smaller loads while frequencies similarly varied. This initial platform may now be used to test various gust cases and fill levels to determine the overall response profiles with the influence of fuel slosh. Subsequently, more meaningful general fuel tank design rules may be developed with ease.

Chapter 7

Summary, Conclusions and Recommendations

7.1 Summary and Conclusions

The aim of this study was to develop a computational loads analysis platform with a high resolution non-linear slosh model included. This is also referred to as a full aircraft model (FAM). This entailed establishing a robust and accurate FSI methodology ensuring strong coupling between fluid and structure. Firstly, the structural ROM was developed so as to integrate with Airbus systems. For this purpose Timoshenko beam theory was employed and Hermitian finite elements used for spatial discretisation. To enable accurate static and dynamic analysis in the time and frequency domain, eigen-analysis procedures were completed for large, sparse matrices. Secondly, the fuel domain was described by the Navier-Stokes set of equations and discretised via the edge-based vertex-centred finite volume method. Lastly, the strongly-coupled fluid-structure interaction scheme was proposed which is tailored for the application under consideration.

The validation and verification of the developed software commenced by evaluating the structure under static and dynamic conditions. For this purpose, various analytical cases were employed as benchmark tests. This ensured a stable, robust and accurate structural ROM was constructed. With regards to the FSI, the proposed solution scheme was assessed against a strongly-coupled analytical test case and exhibited accurate solutions. Finally, the FAM was applied to an actual Airbus wing subjected to a realistic gust load. This was done to evaluate robustness as well as to compare results to the current standard fuel model viz. a full tank.

It was found that the latter over-estimates the structural loads by up to 30% resulting in an over-designed structure. Moreover, the full tank assumption alters the inherent characteristics of the coupled entity by decreasing its natural frequency of vibration by up to 20%. Although the assumption allows for greater loads to be withstood, it neglects the dynamic sloshing effects of fuel. The sloshing fuel impacts the tank walls and may either exacerbate or prohibit motion. The

new FAM takes cognisance of these sloshing effects via the artificial added mass algorithm providing a more accurate slosh representation in real-time. Moreover, the computational platform was found to be robust and stable. The objectives of the study were therefore deemed successfully completed.

7.2 Recommendations

The scope of this study was limited to a non-linear structure in 3D interacting with an incompressible fluid sloshing in two dimensions. The following list includes suggestions to extend this work in the future:

- Further research the frequency domain analysis to aid structural decomposition. This will enable greater integration into current industry methodologies, as well as decrease the simulation time.
- Extend the current beam theory employed to encompass non-linear beam deformation. This provides a more accurate representation of the structural ROM, as well as enabling its application to highly flexible wing structures.
- Extension of the sloshing calculation to 3D. This entails broadening the FSI algorithm and expanding the sloshing solver to three dimensions.
- Import ROMs for sloshing and aerodynamics. The essential aim is to decrease the computational time of a load analysis simulation whilst maintaining the accuracy. Introducing accurate ROMs for the non-linear sloshing component, as well as an accurate non-linear aerodynamic ROM will satisfy the aforementioned aim. Both of these are currently under development at the Industrial CFD research group at the University of Cape Town.

References

- [1] Netjasov, F. and Janic, M. (2008). A review of research on risk and safety modelling in civil aviation. *Journal of Air Transport Management*, 14(4), 213–220.
- [2] Airbus Orders and Deliveries. <http://www.airbus.com/company/market/orders-deliveries> [accessed online: 1 November 2014].
- [3] EASA, C. S. (2013). Acceptable means of compliance for large aeroplanes cs-25. Tech. rep., Tech. Rep. Amendment 13, European Aviation Safety Agency.
- [4] Amsallem, D. and Farhat, C. (2008). Interpolation method for adapting reduced-order models and application to aeroelasticity. *AIAA journal*, 46(7), 1803–1813.
- [5] Bai, Z. (2002). Krylov subspace techniques for reduced-order modeling of large-scale dynamical systems. *Applied Numerical Mathematics*, 43(1), 9–44.
- [6] Lieu, T., Farhat, C., and Lesoinne, M. (2006). Reduced-order fluid/structure modeling of a complete aircraft configuration. *Computer methods in applied mechanics and engineering*, 195(41), 5730–5742.
- [7] Guyan, R. J. (1965). Reduction of stiffness and mass matrices. *AIAA journal*, 3(2), 380–380.
- [8] Wilson, E. L. (1974). The static condensation algorithm. *International Journal for Numerical Methods in Engineering*, 8(1), 198–203.
- [9] Amsallem, D., Cortial, J., Carlberg, K., et al. (2009). A method for interpolating on manifolds structural dynamics reduced-order models. *International journal for numerical methods in engineering*, 80(9), 1241–1258.
- [10] Ibrahim, R. and Woodall, T. (1986). Linear and nonlinear modal analysis of aeroelastic structural systems. *Computers & structures*, 22(4), 699–707.
- [11] Ibrahim, R. A. (2005). *Liquid sloshing dynamics: theory and applications*. Cambridge University Press.

-
- [12] Malan, A. and Oxtoby, O. (2010). A parallel free-surface-modelling technology for application to aircraft fuel-sloshing. In *Proceedings of ECCOMAS CFD-Fifth European Conference on Computational Fluid Dynamics, Lisbon, Portugal*, vol. 14.
- [13] Gambioli, F. (2009). Fuels loads in large civil airplanes. 4th SPHERIC Workshop.
- [14] Dodge, F. T. et al. (2000). *The new dynamic behavior of liquids in moving containers*. Southwest Research Inst. San Antonio, TX.
- [15] Godderidge, B., Turnock, S. R., and Tan, M. (2012). A rapid method for the simulation of sloshing using a mathematical model based on the pendulum equation. *Computers & Fluids*, 57, 163–171.
- [16] Dai, L., Xu, L., and Setiawan, B. (2005). A new non-linear approach to analysing the dynamic behaviour of tank vehicles subjected to liquid sloshing. *Proceedings of the Institution of Mechanical Engineers, Part K: Journal of Multi-body Dynamics*, 219(1), 75–86.
- [17] Higginbotham, S. (2013). *Aircraft Fuel Sloshing Tank Modelling and Characterisation*. Master’s thesis, University of Cape Town.
- [18] Degroote, J., Bathe, K.-J., and Vierendeels, J. (2009). Performance of a new partitioned procedure versus a monolithic procedure in fluid–structure interaction. *Computers & Structures*, 87(11), 793–801.
- [19] Piperno, S., Farhat, C., and Larrouturou, B. (1995). Partitioned procedures for the transient solution of coupled aeroelastic problems part i: Model problem, theory and two-dimensional application. *Computer methods in applied mechanics and engineering*, 124(1), 79–112.
- [20] Le Tallec, P. and Mouro, J. (2001). Fluid structure interaction with large structural displacements. *Computer Methods in Applied Mechanics and Engineering*, 190(24), 3039–3067.
- [21] Felippa, C. A., Park, K., and Farhat, C. (2001). Partitioned analysis of coupled mechanical systems. *Computer methods in applied mechanics and engineering*, 190(24), 3247–3270.
- [22] Wall, W. A., Genkinger, S., and Ramm, E. (2007). A strong coupling partitioned approach for fluid–structure interaction with free surfaces. *Computers & Fluids*, 36(1), 169–183.
- [23] Matthies, H. G. and Steindorf, J. (2003). Partitioned strong coupling algorithms for fluid–structure interaction. *Computers & Structures*, 81(8), 805–812.

- [24] Li, X.-F. (2008). A unified approach for analyzing static and dynamic behaviors of functionally graded timoshenko and euler–bernoulli beams. *Journal of Sound and vibration*, 318(4), 1210–1229.
- [25] Timoshenko, S. P. (1921). Lxvi. on the correction for shear of the differential equation for transverse vibrations of prismatic bars. *The London, Edinburgh, and Dublin Philosophical Magazine and Journal of Science*, 41(245), 744–746.
- [26] Song, S. and Waas, A. (1997). Effects of shear deformation on buckling and free vibration of laminated composite beams. *Composite Structures*, 37(1), 33–43.
- [27] Han, S. M., Benaroya, H., and Wei, T. (1999). Dynamics of transversely vibrating beams using four engineering theories. *Journal of Sound and Vibration*, 225(5), 935–988.
- [28] Cowper, G. (1966). The shear coefficient in timoshenko’s beam theory. *Journal of applied mechanics*, 33(2), 335–340.
- [29] Hutchinson, J. (2001). Shear coefficients for timoshenko beam theory. *Journal of Applied Mechanics*, 68(1), 87–92.
- [30] Timoshenko, S. and Goodier, J. Theory of elasticity, 1951. *New York*, 412.
- [31] Przemieniecki, J. S. (1985). *Theory of matrix structural analysis*. Courier Dover Publications.
- [32] Suliman, R., Oxtoby, O., Malan, A., et al. (2014). A matrix free, partitioned solution of fluid–structure interaction problems using finite volume and finite element methods. *European Journal of Mechanics-B/Fluids*.
- [33] Bathe, K.-J. (2008). *Finite element method*. Wiley Online Library.
- [34] Zienkiewicz, O. C. and Taylor, R. L. (2005). *The finite element method for solid and structural mechanics*. Butterworth-heinemann.
- [35] Cook, R. D. et al. (2007). *Concepts and applications of finite element analysis*. John Wiley & Sons.
- [36] Bathe, K.-J. and Wilson, E. L. (1976). Numerical methods in finite element analysis.
- [37] Saad, Y. (1992). *Numerical methods for large eigenvalue problems*, vol. 158. SIAM.
- [38] Liu, M. and Gorman, D. (1995). Formulation of rayleigh damping and its extensions. *Computers & structures*, 57(2), 277–285.

- [39] Caughey, T. and O'Kelly, M. (1965). Classical normal modes in damped linear dynamic systems. *Journal of Applied Mechanics*, 32(3), 583–588.
- [40] Clark, P., Aiken, I., Kasai, K., et al. (1999). Design procedures for buildings incorporating hysteretic damping devices. In *Proceedings 68th annual convention*. pp. 355–371.
- [41] Krenk, S. (2001). *Mechanics and analysis of beams, columns and cables: a modern introduction to the classic theories*. Springer.
- [42] Greenshields, C. and Weller, H. (2005). A unified formulation for continuum mechanics applied to fluid–structure interaction in flexible tubes. *International Journal for Numerical Methods in Engineering*, 64(12), 1575–1593.
- [43] Rao, S. S. (2007). *Vibration of continuous systems*. John Wiley & Sons.
- [44] Causin, P., Gerbeau, J.-F., and Nobile, F. (2005). Added-mass effect in the design of partitioned algorithms for fluid–structure problems. *Computer methods in applied mechanics and engineering*, 194(42), 4506–4527.
- [45] Degroote, J., Annerel, S., and Vierendeels, J. (2010). Stability analysis of gauss–seidel iterations in a partitioned simulation of fluid–structure interaction. *Computers & structures*, 88(5), 263–271.
- [46] Mowat, A. G. B., Van Den Bergh, W. J., Malan, A. G., et al. (2015). An algebraic multigrid solution strategy for efficient solution of free-surface flows. *International Journal of Computational Fluid Dynamics*. Submitted for review.
- [47] Malan, A. and Oxtoby, O. (2010). A parallel free-surface-modelling technology for application to aircraft fuel-sloshing. In *Proceedings of ECCOMAS CFD-Fifth European Conference on Computational Fluid Dynamics, Lisbon, Portugal*, vol. 14.
- [48] Förster, C., Wall, W. A., and Ramm, E. (2007). Artificial added mass instabilities in sequential staggered coupling of nonlinear structures and incompressible viscous flows. *Computer methods in applied mechanics and engineering*, 196(7), 1278–1293.
- [49] Suliman, R., Oxtoby, O., Malan, A., et al. (2012). Development of a partitioned finite volume-finite element fluid-structure interaction scheme for strongly-coupled problems.
- [50] Bathe, K.-J. and Ledezma, G. A. (2007). Benchmark problems for incompressible fluid flows with structural interactions. *Computers & structures*, 85(11), 628–644.